creative commons

COMMONS DEED

저작자표시-비영리-변경금지 2.0 대한민국

이용자는 아래의 조건을 따르는 경우에 한하여 자유롭게

- 이 저작물을 복제, 배포, 전송, 전시, 공연 및 방송할 수 있습니다.

다음과 같은 조건을 따라야 합니다:

저작자표시. 귀하는 원저작자를 표시하여야 합니다.

비영리. 귀하는 이 저작물을 영리 목적으로 이용할 수 없습니다.

변경금지. 귀하는 이 저작물을 개작, 변형 또는 가공할 수 없습니다.

- 귀하는, 이 저작물의 재이용이나 배포의 경우, 이 저작물에 적용된 이용허락조건을 명확하게 나타내어야 합니다.
- 저작권자로부터 별도의 허가를 받으면 이러한 조건들은 적용되지 않습니다.

저작권법에 따른 이용자의 권리는 위의 내용에 의하여 영향을 받지 않습니다.

이것은 이용허락규약(Legal Code)을 이해하기 쉽게 요약한 것입니다.

Disclaimer

dCollection

[UCI]I804:31001-200000223960

ULSAN NATIONAL INSTITUTE OF
SCIENCE AND TECHNOLOGY

Comparison of Thermoelastic Micromechanical Response of Polycrystalline Microstructures using Finite Element Method and Fast Fourier Transform-based Method

Myeong-jin Lee

Department of Materials Science and Engineering

Graduate School of UNIST

ULSAN NATIONAL INSTITUTE OF
SCIENCE AND TECHNOLOGY

Comparison of Thermoelastic Micromechanical Response of Polycrystalline Microstructures using Finite Element Method and Fast Fourier Transform-based Method

A thesis/dissertation
submitted to the Graduate School of UNIST
in partial fulfillment of the
requirements for the degree of
Master of Science

Myeong-jin Lee

7. 12. 2019
Approved by

_____

Advisor
Prof. Sukbin Lee

ULSAN NATIONAL INSTITUTE OF SCIENCE AND TECHNOLOGY

Comparison of Thermoelastic Micromechanical Response of Polycrystalline Microstructures using Finite Element Method and Fast Fourier Transform-based Method

Myeong-jin Lee

This certifies that the thesis/dissertation of Myeong-jin Lee is approved.

7/12/2019

signature

_____

Advisor: Prof. Sukbin Lee

signature

_____

Prof. KiSuk Lee

signature

_____

Prof. Ju-Young Kim

signature

_____

ULSAN NATIONAL INSTITUTE OF
SCIENCE AND TECHNOLOGY

Abstract

A comparison of the results from the finite element method (FEM) and fast Fourier transform-based (FFT) method, was carried out in the context of the thermoelasticity. In order to validate and compare each numerical method, the thermoelastic response of heterogeneous materials system, the Eshelby's inclusion problem was adopted. Both similarity and discrepancy of the thermoelastic responses between two methods were examined. It was found that both methods showed similar trends in predicting average values of mechanical response, however, produced quite a big discrepancy at the particle-matrix boundary regions. This result will raise the question that which method predicts better response of thermoelasticity for a three-dimensional polycrystalline material under thermal loading, where, especially, the extreme values (i.e., hot spots in stress) are preferentially located around the grain boundary regions and eventually cause the failure of rather brittle polycrystalline materials.
Keywords: Thermoelasticity; Finite element method; fast Fourier transform-based method; Polycrystal

ULSAN NATIONAL INSTITUTE OF
SCIENCE AND TECHNOLOGY

ULSAN NATIONAL INSTITUTE OF SCIENCE AND TECHNOLOGY

Contents

I. Introduction 1

II. Theoretical Background 2

2.1 Thermoelasticity 2
2.2 Thermoelastic FEM 5
2.3 Thermoelastic FFT 6
2.4 Extreme Value Analysis 8
2.4.1 Introduction to Extreme Value Analysis 9

III. Eshelby's Inclusion Problem 11

3.1 Introduction 11
3.2 Simulation parameters 11
3.3 Results & Discussion 12
3.3.1. Stress distribution 13
3.3.2 Stress profiles 13

IV. Thermoelastic Response of a Polycrystalline Material 17

4.1 Introduction 17
4.2 Model description 17
4.3 Isotropic Case 18
4.3.1 Material Selection 18
4.3.2 Comparison of local response: von Mises equivalent stress distribution 18
4.3.2 Statistical Extreme value Techniques 22
4.4 Anisotropic Case 25
4.4.1 Material Selection 25
4.4.2 von Mises equivalent stress distribution 25
4.4.3 Application of Eshelby problem to anisotropic case 26

V. Conclusion 30

REFERENCES 31

ULSAN NATIONAL INSTITUTE OF SCIENCE AND TECHNOLOGY

List of figures

Figure 1. Two widely used methodology in extreme value analysis. (a) Block maxima and (b) Peaks-over-threshold (POT).

Figure 2. Generated 3D input microstructure with spherical inclusion (red) embedded in an infinite matrix (white in left, gray in right) is discretized on a regular voxel grid (a),(b) 32×32×32 and (c),(d) 64×64×64.

Figure 3. Stress field on cross section (the section in the middle of z-axis with x-axis horizontal, y-axis vertical) predicted with TE-FEM and TE-FFT for a 32×32×32 resolution. $\sigma 11$ distribution resulting from (a) TE-FEM, (b) TE-FFT, and (c) differences between each method are shown. (d)-(e) are corresponding distribution of $\sigma 22$.

Figure 4. Stress field on cross section predicted with TE-FEM and TE-FFT for a 64×64×64 resolution. $\sigma 11$ distribution resulting from (a) TE-FEM, (b) TE-FFT, and (c) differences between each method are shown. (d)-(e) are corresponding distribution of $\sigma 22$.

Figure 5. Profiles resulting from TE-FEM (red open circle) and TE-FFT (blue open circle) for 32×32×32 resolution on stress profile calculated from Eshelby (black solid line).

Figure 6. Profiles resulting from TE-FEM (red open circle) and TE-FFT (blue open circle) for 64×64×64 resolution on stress profile calculated from Eshelby (black solid line).

Figure 7. (a) A generated hypothetical 3D microstructure with size 64×64×64 and (b) its corresponding normalized grain size distribution.

Figure 8. Stress field (von Mises equivalent stress) on the cross section of the microstructure. (a) prediction from TE-FEM for random orientation set 1 to 5, respectively, and (b) displays relative results from TE-FFT.

Figure 9. (a) Calculated differences in stress between two methods. When TEFEM prediction is higher than TEFFT prediction, stress field is identified as red, and, represented as blue for the opposite case. (b) Percent error calculated from absolute value of differences divided by stress values from FFT prediction times 100.

Figure 10. (a) Scatter plot and (b) box plot of stress versus normalized grain size

Figure 11. The ratio of stress resulting from two methods versus grain size

Figure 12. Probability density functions for stress resulting from TE-FEM (red) and TE-FFT (blue)

Figure 13. Probability plots of normalized stress resulting from TE-FEM (red) and TE-FFT (blue)

Figure 14. Threshold choice plots and mean residual life plots for the stress resulting from (a) TE-FEM and TE-FFT.

Figure 15. Diagnostic plots for the fitted GPD

ULSAN NATIONAL INSTITUTE OF
SCIENCE AND TECHNOLOGY

Figure 16. Stress fields on the cross section of the microstructure. (a) prediction from TE-FEM for random orientation set 1 to 5, respectively, and (b) displays relative results from TE-FFT.

Figure 17. Calculated differences (Subtraction of TE-FFT results from TE-FEM prediction) in stress between two methods. (b) shows corresponding percent error which are calculated from absolute value of differences divided by stress values from FFT prediction times 100.

Figure 18. Probability distribution function for stress resulting from TE-FEM (red) and TE-FFT (blue).

Figure 19. Stress field on cross section resulting from TE-FEM, TE-FFT (left) and relative profiles compared to Eshelby case for isotropic case.

Figure 20. Stress field on cross section resulting from TE-FEM, TE-FFT (left) and relative profiles compared to Eshelby case for anisotropic case.

ULSAN NATIONAL INSTITUTE OF
SCIENCE AND TECHNOLOGY

List of Tables

Table 1.The average and standard deviation of $\boldsymbol{\sigma_{11}}$ and $\boldsymbol{\sigma_{22}}$ distribution inside the inclusion. The analytical value measured by Eshelby's theory is 376.05 MPa

Table 2.The simulation time for computing Eshelby problem.

Table 3. Descriptive statistics for stress for all five sets of test microstructure for isotropic case.

Table 4. Statistics for the stress data sets from TE-FEM and TE-FFT

Table 5.Descriptive statistics for stress for all five sets of test microstructure for anisotropic case.

ULSAN NATIONAL INSTITUTE OF SCIENCE AND TECHNOLOGY

I. Introduction

In polycrystalline materials under varied temperatures, are induced thermal stresses due to the crystallographic anisotropy and spatial distribution of grains and grain boundary network. At the microstructural scale, localization of such stress can be the source of failures such as cracking [1, 2]. For this reason, the investigation of extreme values of local distribution of mechanical fields is of a great interest in predicting life time and evaluating the safety of many engineering materials and its applications [3]. Robust modeling and simulation techniques have been extensively used to quantify the mechanical behavior of the materials systems in that regard [4]. Such numerical methods are categorized as mean-field models and full-field models [3, 4]. The mean-field models employ homogenization schemes such as Sachs [5] and Taylor [6], in which, equal stress and strain in the constituents are assumed, respectively [7]. Likewise, Eshelby [8] proposed stress and strain equilibrium of an ellipsoidal inclusion in a matrix with respect to the homogeneous far-field of stress and strain. More recently, self-consistent models are used to find a solution, e.g. Molinari et al [9], Lebensohn and Tomé [10]. The mean-field method is known to be more efficient compared to the full-field method in the aspect of computational time. However, most of the models above mentioned have shortcomings, which is the overestimation of the texture and anisotropy [4].

The first study of full-field method was presented in terms of crystal plasticity finite element simulation (CPFEM) by Peirce et al [11]. The full-field method indicates consideration of short- and long-range grain interactions as well as a resolution of micromechanical properties on discretized grid [12]. Thereby, full-field simulation can provide a more accurate description of micromechanical fields in polycrystals and can give information upon stress and strain distribution inside the grains or in the vicinity of grain boundaries [3, 4]. For complex and anisotropic polycrystals, more realistic modeling of geometry and finely discretized elements are needed, and, finite element method (FEM) has widely been adopted to compute this type of problems. However, it is difficult to obtain appropriate mesh for FEM simulation and needs large number of degrees of freedom as well, which in turn leads to the limitation of modeling size and considerable computational time [13]. From this point of view, fast Fourier transform (FFT) can be suggested as an alternative method by virtue of finely discretized mesh free elements [14, 15]. The full-field method based on FFT was originally developed by Moulinec and Suquet to solve micromechanical properties for linear elastic response of composite materials and then expanded to inelastic region [15-18]. This FFT-based approach has been successfully applied to the field of elastic [19], thermoelastic [20], viscoplastic [14] and elasto-viscoplastic [3] models. As the FFT algorithm is a mesh free method, meshing problem can be avoided, and the memory for solving the computation can be reduced [4, 21]. The limitation of FFT method is the boundary conditions, as it is restricted to have periodic boundary conditions only.

Recently, full-field methods based on FEM and FFT approaches has been compared for elastic, viscoplastic and elasto-viscoplastic models [4, 12, 14]. Previous studies indicated that predictions by

ULSAN NATIONAL INSTITUTE OF SCIENCE AND TECHNOLOGY

both methods exhibit similar trends in macroscopic response and show little difference between two methods in average stress/strain distribution. While fundamental comparisons have been provided in previous work, substantial statistical information regarding thermoelasticity is not yet discussed, hence, one has to give efforts on studying statistical information to understand and compare the response of the momentous extreme values, i.e. extremely high values of local responses (or hot spots). Hot spot stress or elastic strain energy density (EED) existing in the upper tail of the distribution are the main areas of our interest, because of their significant role in creep and fatigue characteristics under temperature variation. In this respect, differences between FEM and FFT in predicting elastic response under thermal loading were investigated with respect to the upper tail, by reference to the extreme value theory, so as to verify the similarities and distinctiveness of both methods.

The proposed research is conducted as follows. First, stress distributions resulting from FE and FFT methods are validated by comparing against analytical solution of Eshelby's problem for a spherical inclusion embedded in an infinite matrix [8]. Then, elastic local fields of polycrystal under thermal loading with properties of cubic/HCP material were explored. Since the input microstructure is configured as individual grains with different size and shape, heterogeneous stiffness tensor and coefficient of thermal expansion (CTE) give rise to inhomogeneous elastic fields distribution inside the grains and near the grain boundaries. For isotropic case with cubic crystal structure, differences are analyzed with respect to the extreme value theory. For anisotropic case with HCP crystal structure, Eshelby's problem is applied to investigate the effect of anisotropy in more detail. By doing so, similarities and distinctiveness in elastic response between FEM and FFT are quantified.

II. Theoretical Background

2.1 Thermoelasticity

The theory of thermoelasticity dealt with strain in an elastic body with thermal expansion. The relationship between stress and strain in terms of temperature variation is described by the generalized Hooke's law including tensor-valued quantities of stiffness and CTE, which implies the effect of crystallographic anisotropy on thermoelastic properties [22]. Anisotropy, particularly the thermal expansion anisotropy can lead to the development of heterogeneous thermal stress, strain, and strain energy density distributions, which are related to the mechanical properties directly.

2.1.1 Moduli of Thermoelasticity

When thermal loading is imposed to a solid body, the majority of the bodies increase in their volume, and such characteristics are known as thermal expansion. In order to define thermoelastic deformation, the CTE tensor, α_{ij}, and thermal loading, ΔT appear in the equation [23] as:

ULSAN NATIONAL INSTITUTE OF SCIENCE AND TECHNOLOGY

$$\varepsilon_{ij}^{thermal} = \alpha_{ij}\Delta T \tag{1}$$

The above equation describes the relationship between the small temperature change and the thermal eigenstrain in the solid. As the CTE tensor (α_{ij}) connects the symmetric second rank tensor (ε_{ij}) and scalar quantity (ΔT), it is understandably symmetric second rank tensor. For cubic crystals, CTE has only the single coefficient (α_{11}) which signifies the expansion or contraction of material occurs in all crystallographic directions at the same rate. On the other hand, for hexagonal crystals with anisotropic CTE, two principal axial coefficients (α_{11}, α_{33}) are necessary. The CTE tensors of Cubic and hexagonal crystals are represented in the form [23]:

$$\text{Cubic} = \begin{pmatrix} \alpha_{11} & 0 & 0 \\ 0 & \alpha_{11} & 0 \\ 0 & 0 & \alpha_{11} \end{pmatrix}, \ \text{Hexagonal} = \begin{pmatrix} \alpha_{11} & 0 & 0 \\ 0 & \alpha_{11} & 0 \\ 0 & 0 & \alpha_{33} \end{pmatrix} \tag{2}$$

In the above expression, α_{11} coefficient indicates a-axis thermal expansion coefficient (α^a) implying the expansion in basal plane, and α_{33} coefficient represents c-axis thermal expansion coefficient (α^c) designating expansion in axial direction. The anisotropy of thermal expansion (α^{aniso}) can be described by the equation below [24]:

$$\alpha^{aniso} = \frac{\alpha^c}{\alpha^a} \tag{3}$$

A basic formula of material property is described as generalized Hooke's law. Assume that tensile load F is applied to a bar of an isotropic material, consisting of initial area and length as A_0 and l_0, respectively. The elongation Δl can be expressed as $\Delta l = Fl_0/EA_0$, where E is the elastic modulus (also known as stiffness constant, C). Stress, the force per unit area on a body can be designated as $\sigma = F/A_0$, and, corresponding elastic longitudinal strain is $\varepsilon = l/l_0$. By considering these equations, a basic formula of elastic deformation can be expressed as Hooke's law [22].

$$\sigma = C\varepsilon \tag{4}$$

For an anisotropic case, this relation of stress and strain is generalized as:

$$\sigma_{ij} = C_{ijkl}\varepsilon_{kl}^{elastic} \tag{5}$$

ULSAN NATIONAL INSTITUTE OF SCIENCE AND TECHNOLOGY

In above equation, C_{ijkl} is a fourth rank stiffness tensor of material properties having 81 (3×3×3×3) components which relates two symmetric second rank tensor, σ_{ij} and $\varepsilon_{kl}^{elastic}$. As the symmetry of the stress tensor reduces the number of such components, we can obtain:

$$\begin{gathered}\sigma_{ij} = \sigma_{ji}\ , \\ \sigma_{ij} = C_{ijkl}\varepsilon_{kl} = C_{jikl}\varepsilon_{kl}\end{gathered} \tag{6}$$

Similarly, the symmetry of the strain tensor also reduces the number of components as follows:

$$\begin{gathered}\varepsilon_{kl} = \varepsilon_{lk}\ , \\ \sigma_{ij} = C_{ijkl}\varepsilon_{kl} = C_{ijlk}\varepsilon_{lk}\end{gathered} \tag{7}$$

By means of eqs.(6) and (7), following form can be obtained:

$$C_{ijkl} = C_{jikl} = C_{ijlk} \tag{8}$$

Consequently, by exploiting the above relationship and imposing crystal symmetries, the number of reduced components is 36, and its matrix form can be written as:

$$\begin{pmatrix}\sigma_1\\ \sigma_2\\ \sigma_3\\ \sigma_4\\ \sigma_5\\ \sigma_6\end{pmatrix} = \begin{pmatrix}C_{11} & C_{12} & C_{13} & C_{14} & C_{15} & C_{16}\\ C_{11} & C_{22} & C_{23} & C_{24} & C_{25} & C_{26}\\ C_{13} & C_{23} & C_{33} & C_{34} & C_{35} & C_{36}\\ C_{14} & C_{24} & C_{34} & C_{44} & C_{45} & C_{46}\\ C_{15} & C_{25} & C_{35} & C_{45} & C_{55} & C_{56}\\ C_{16} & C_{26} & C_{36} & C_{46} & C_{56} & C_{66}\end{pmatrix}\begin{pmatrix}\varepsilon_1\\ \varepsilon_2\\ \varepsilon_3\\ \varepsilon_4\\ \varepsilon_5\\ \varepsilon_6\end{pmatrix} \tag{9}$$

Meanwhile, the total strain induced by the stress σ and temperature variation is expressed as the sum of the elastic strains and thermal eigenstrains as:

$$\varepsilon^{total} = \varepsilon^{elastic} + \varepsilon^{thermal} = \varepsilon^{elastic} + \alpha\Delta\mathrm{T} \tag{10}$$

Hence, the anisotropic elasticity can be expressed as:

$$\begin{gathered}\sigma_{ij} = C_{ijkl}\varepsilon_{kl}^{elastic} \\ = C_{ijkl}(\varepsilon_{kl}^{total} - \varepsilon^{thermal}) = C_{ijkl}(\varepsilon_{kl}^{total} - \alpha_{kl}\Delta\mathrm{T})\end{gathered} \tag{11}$$

ULSAN NATIONAL INSTITUTE OF SCIENCE AND TECHNOLOGY

2.2 Thermoelastic FEM

The FEM approach is recognized as one of the powerful numerical methods that can be applied to numerous engineering analyses [25, 26]. Generally, it is not a simple task to solve an analytical solution satisfying the variational equations. For this reason, the FEM uses an approximation solution. As its name suggests, the FEM discretizes a domain (i.e. microstructure) into a number of simple-shaped finite elements. The domain integral of the weak field equation is then decomposed into integrals over each element, and, the solution is approximated by means of a simple polynomial form in the element. Thereby, the governing equations of the entire domain can be derived. Since the elements are connected with adjacent elements by sharing their nodes, adjacent elements have the same solution value at the shared nodes.

In using the FEM, formulation of a linear or nonlinear system is considered and can be expressed as a matrix form, implying the forces acting on the elements are product of stiffness matrix and nodal displacement vector as [27]:

$$K_{ij}u_j = F_i \text{ or } \boldsymbol{Ku} = \boldsymbol{F} \tag{12}$$

where K_{ij} is global stiffness matrix, u_j is the deflection at j^{th} node and F_i is the force at the ith node. The corresponding boldface denotes the matrix quantities for the system. As eq.(12) is similar to the linear relationship between stress and strain in eq.(11), adjustment can be made at the element level:

$$\{\bar{f}^{(e)}\} = [\bar{k}^{(e)}]\{\bar{q}^{(e)}\} - \{\bar{f}_T^{(e)}\} \tag{13}$$

The element thermal force vector $\bar{f}_T^{(e)}$ can be expressed as:

$$\left\{\bar{f}_T^{(e)}\right\} = AE\alpha\Delta T \begin{Bmatrix} -1 \\ 0 \\ +1 \\ 0 \end{Bmatrix} \begin{matrix} \bar{u}_i \\ \bar{v}_i \\ \bar{u}_j \\ \bar{v}_i \end{matrix} \tag{14}$$

In eq.(14), row addresses on the right-hand indicate the degrees of the freedom(DOF) corresponding to each force. The relationship between local and global displacements can be expressed by introducing the transformation matrix, $[T]$:

$$\{\bar{q}\} = [T]\{q\} \tag{15}$$

ULSAN NATIONAL INSTITUTE OF SCIENCE AND TECHNOLOGY

Using the transpose of the transformation matrix $[T]^T$ yields

$$\{f\} = [k]\{q\} - \{f_T\} \tag{16}$$

And, the global equations at the structural level is obtained as:

$$[K_s]\{Q_s\} = \{F_s\} + \{F_{Ts}\} \tag{17}$$

Here, $\{F_{Ts}\}$ is the thermal load vector determined by assembling $\{f_T\}$ in the elements. By substituting and striking out equations with zero DOFs, the global equations are obtained as:

$$[K]\{Q\} = \{F\} + \{F_T\} \tag{18}$$

In using the FEM for thermoelasticity, finding the numerical approximation to the analytical solution can be stated as solving unknown displacement $\{Q\}$, maintaining the momentum of thermoelasticity.

2.3 Thermoelastic FFT

The fundamental framework of FFT was supposed by Moulinec and Suquet [15-17] giving us guidance for introducing the solution of the local problem of an inhomogeneous elastic medium. For the FFT-based method, on the contrary to FEM, a periodic unit cell (i.e. microstructure) is introduced, which are discretized into Fourier points, on behalf of a regular grid $\{\mathbf{x}\}$. By considering a homogeneous reference medium with stiffness ${C_{ijkl}}^0$ subject to a periodic polarization field $\tau_{ij}(\mathbf{x})$, the linear elasticity relationship in eq.(11) can be transformed into:

$$\sigma_{ij}(\mathbf{x}) = {C_{ijkl}}^0(\mathbf{x})\varepsilon_{kl}(\mathbf{x}) + \tau_{ij}(\mathbf{x}) \tag{19}$$

In the above equation, the polarization field is given by:

$$\tau_{ij}(\mathbf{x}) = \left(C_{ijkl}(\mathbf{x}) - C^0_{ijkl}\right)\varepsilon_{kl}(\mathbf{x}) - C_{ijkl}(\mathbf{x})\varepsilon^*_{kl}(\mathbf{x}) \tag{20}$$

where $\varepsilon_{kl}(\mathbf{x})$ and $\varepsilon^*_{kl}(\mathbf{x})$ is total strain (ε^{total}_{kl}) and thermal eigen strain ($\varepsilon^{thermal}$), respectively. Since the strain field is related to the displacement field $u_k(\mathbf{x})$ as:

ULSAN NATIONAL INSTITUTE OF SCIENCE AND TECHNOLOGY

$$\varepsilon_{kl}(\mathbf{x}) = \frac{\left(u_{k,l}(\mathbf{x}) + u_{l,k}(\mathbf{x})\right)}{\mathbf{2}} \tag{21}$$

and $\sigma_{ij,j}(\mathbf{x})$ is equal to zero for equilibrium, eq.(19) is transformed into:

$$C^0_{ijkl} u_{k,lj}(\mathbf{x}) + \tau_{ij,j}(\mathbf{x}) = 0 \tag{22}$$

By means of the Green's function $G_{km}(\mathbf{x} - \mathbf{x}')$, following equation can be obtained.

$$C^0_{ijkl} G_{km,lj}(\mathbf{x} - \mathbf{x}') + \delta_{im}\delta(\mathbf{x} - \mathbf{x}') = 0 \tag{23}$$

If $G_{km}(\mathbf{x})$ is known, eq.(22) can be rewritten with respect to the local fluctuation of the displacement field as:

$$u_k = \int_V G_{ki}(\mathbf{x} - \mathbf{x}')\, \tau_{ij,j}(\mathbf{x}')\mathrm{d}\mathbf{x}' \tag{24}$$

In Fourier space $\{\mathbf{k}\}$, the convolution integral in eq.(24) can be simplified by using Γ_{ijkl}=sym($G_{ik,jl}$):

$$\hat{u}_{i,j}(\mathbf{k}) = \hat{\Gamma}_{ijkl}(\mathbf{k})\hat{\tau}_{kl}(\mathbf{k}) \text{ for } \mathbf{k} \neq 0, \text{ and } \hat{u}_{i,j}(\mathbf{0}) = E_{ij} \tag{25}$$

where "^" signifies the Fourier transform and E_{ij} represents the macroscopic strain applied to the unit cell. By means of Eqs. (24) and (25), operators can be calculated as:

$$\begin{gathered} \hat{G}_{ij}(\mathbf{k}) = A^{-1}_{ij}(\mathbf{k}), \text{ where } A_{ij}(\mathbf{k}) = k_j k_i C^0_{ijkl}, \\ \text{and } \hat{\Gamma}_{ijkl}(\mathbf{k}) = -k_j k_i \hat{G}_{ij}(\mathbf{k}) \end{gathered} \tag{26}$$

Since the polarization field in real space $\tau_{ij}(\mathbf{x})$ is unknown, $\varepsilon_{ij}(\mathbf{x})$ is guessed by using anti-transformation and symmetrization of eq.(25), and then applied to eq.(20) to determine a new guess of the polarization field. Iterations for thermoelastic problem in terms of macroscopic strain is given according to [14, 28]:

$$E^{(i)}_{ij} = \langle \varepsilon^{(i)}_{ij}(\mathbf{x}) \rangle - C^{0^{-1}}_{ijkl} \langle \sigma^{(i)}_{kl}(\mathbf{x}) \rangle \tag{27}$$

where $\langle \cdot \rangle$ denotes average over the entire grid in Cartesian space. Such iterative procedure is converged

ULSAN NATIONAL INSTITUTE OF SCIENCE AND TECHNOLOGY

when the total strain field fulfil the appropriate tolerance of the output field. The error criterion for convergence test is:

$$err^{(i+1)} = \frac{\langle \| \varepsilon_{ij}^{(i+1)}(\mathbf{x}) - \varepsilon_{ij}^{(i)}(\mathbf{x}) \| \rangle}{\| E_{ij}^{(i+1)} \|} \tag{28}$$

If error is smaller than tolerance (i.e., equilibrium condition is fulfilled), simulation is completed.
In summary, the algorithm begins by initialization as:

1. Computation: $E_{ij}^{(0)} = \langle \varepsilon_{ij}^{*}(\mathbf{x}) \rangle$
2. Allocation: $\varepsilon_{ij}^{(0)}(\mathbf{x}) = E_{ij}^{(0)}$
3. Computation: $\mathrm{sym}(\hat{\Gamma}_{ijkl}(\mathbf{k}))\forall\mathbf{k}$

when $E_{ij}^{(i)}$ and $\varepsilon_{ij}^{(i)}(\mathrm{x})$ are known, iteration (i+1) begins:

1. Calculate the polarization field at (i+1): $\tau_{ij}^{i+1}(\mathbf{x}) = \left(C_{ijkl}(\mathbf{x}) - C_{ijkl}^{0}\right)\varepsilon_{kl}^{(i)}(\mathbf{x}) - C_{ijkl}(\mathbf{x})\varepsilon_{kl}^{*}(\mathbf{x})$
2. Fourier transformation of polarization field: $\hat{\tau}^{i+1}(\mathbf{x}) = \mathrm{FFT}(\tau^{i+1}(\mathbf{x}))$
3. Compute strain field: $\varepsilon_{ij}^{(i+1)}(\mathbf{x}) = E_{ij}^{(i)} + \mathrm{FFT}^{-1}(\mathrm{sym}(\hat{\Gamma}_{ijkl}(\mathbf{k}))\, \hat{\tau}_{kl}^{(i+1)}(\mathbf{k}))(\mathbf{x})$
4. Compute constitutive equation: $\sigma_{ij}^{(i+1)}(\mathbf{x}) = C_{ijkl}(\mathbf{x})(\varepsilon_{kl}^{(i+1)}(\mathbf{x}) - \varepsilon_{kl}^{*}(\mathbf{x}))$
5. Applying boundary condition: $E_{ij}^{(i+1)} = \langle \varepsilon_{ij}^{(i+1)}(\mathbf{x}) \rangle - C_{ijkl}^{0^{-1}} \langle \sigma_{kl}^{(i+1)}(\mathbf{x}) \rangle$
6. Finally, convergence test is performed using error criterion:

2.4 Extreme Value Analysis

In this work, we focused on a method of data analysis by reference to the statistical extreme value analysis. Conventionally, prediction of mechanical response using numerical simulation usually relied on the incomplete descriptions, such as histogram, or concentrated on the average and standard deviation of data, ignoring the extreme values existing in the upper/lower tail of the distribution. Even though such descriptions provide the fundamental information of the stress and strain range from simulations, one has to give efforts on studying substantial statistical information to understand the momentous upper tail values, for instance, hot spot stress. As tail values have significant influences on material's behavior, for instance, creep and fatigue damage, it is required to analyze the extreme values when modelling the materials [29-31].

ULSAN NATIONAL INSTITUTE OF SCIENCE AND TECHNOLOGY

2.4.1 Introduction to Extreme Value Analysis

In the extreme value analysis, most commonly used approaches to define extreme values are the block maxima and the peaks-over-threshold (POT) approach [32]. The first method, in the block maxima approach, data sets are divided into bins of equal size, and extreme values are defined as the maximum of each predefined interval (such as regional annual maxima of rainfall) as illustrated in Fig.1 (a). The second method, so called the POT approach, the extreme events are determined as all data sets exceeding threshold value as depicted in Fig.1 (b). The extreme events selected by means of these methods are expressed as full red circle. By using the POT analysis, many of authors have estimated large natural catastrophes such as extreme wind, wave, rainfall and earthquake events [33-36]. Since our areas of interests, the extreme values (hot spot) of stress are not a time series, and, our main concern is to examine the single data sets above the threshold, the POT approach is chosen for this study.

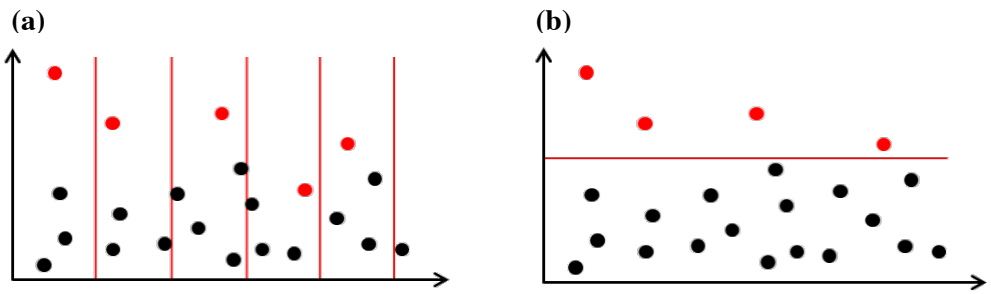

Figure 1. Two widely used methodology in extreme value analysis. (a) the Block maxima and (b) the Peaks-over-threshold (POT).

Suppose $X_1, X_2, \dots, X_n$ are independent and identically distributed random variables, having marginal distribution function F. First of all, choose a sufficiently high threshold u to determine the extreme values X_i which exceed the threshold call. The idea of the POT method is that the stochastic behavior of distribution tail can be described as a conditional probability function [29, 37]:

$$F_u(x) = P(X - u \leq x \mid X > u) = \frac{F(u + x) - F(u)}{1 - F(u)} \tag{29}$$

The framework for the POT approach is provided by Pickands-Balkema-de Haan theorem which states that the distribution F_u in eq.(29) converges to the generalized Pareto distribution (GPD) as threshold u approaches right end point, simplified as:

$$F_u(x) \to G_{\xi,\sigma}(x) \text{ as } u \to \infty \tag{30}$$

where $G_{\xi,\sigma}$ implies the GPD, u, σ and ξ are the location, scale, and shape parameters, respectively. The

ULSAN NATIONAL INSTITUTE OF SCIENCE AND TECHNOLOGY

GPD, a family of continuous probability distribution being used to statistical assessment of the distribution tail can be formulated as [29]:

$$G_{\xi,\mu,\sigma}(x) = \begin{cases} 1 - \left(1 + \frac{\xi(x-\mu)}{\sigma}\right)^{-\frac{1}{\xi}} & if\ \xi \neq 0 \\ 1 - \exp\left(-\frac{x-\mu}{\sigma}\right) & if\ \xi = 0 \end{cases} \tag{31}$$

The associated three parameters of the GPD has significant role, where shape (ξ) parameter indicates spread, scale (σ) parameter implies length, and location (u) parameter signifies the threshold of tail distribution. It is notable that σ and ξ are functions of the threshold (μ), so that the properties of these estimators significantly depend on the behavior of distribution tail. The methodology is based on the assumption that excesses over high threshold can be approximated by the GPD. By fitting the data to the GPD, the threshold exceedances (i.e., extreme values) of data are characterized. Description in more detail can be found in [29].

2.4.2 Tail Fitting using Extreme Value Analysis

To discriminate extreme values as well as to choose a threshold, two useful graphical tools, the threshold choice plot and mean residual life plot were used [38].

The threshold choice plot gave us a guidance for selecting excesses, regarding the stability property of the GPD. If the GPD is appropriate for excesses over the threshold u_0, then it is also reasonable for another threshold $u > u_0$. The parameterization of updated value can be expressed as:

$$\sigma_1 = \sigma_0 + \xi_0(\mu_1 - \mu_0) \text{ and } \xi_0 = \xi_1 \tag{32}$$

By introducing a new parameter σ_* as:

$$\sigma_* = \sigma_1 - \xi_1\mu_1 \tag{33}$$

then, σ_* is independent of μ_0, and accordingly, σ_* and ξ_1 are constant above μ_0. It implies that resulting threshold choice plot will be stable with reasonable threshold call.

In the mean residual plot, the expected value of excesses can be represented as:

$$E[X - \mu | X > \mu] = \frac{\sigma_{\mu_0} + \xi\mu}{1 - \xi} \tag{34}$$

ULSAN NATIONAL INSTITUTE OF SCIENCE AND TECHNOLOGY

Where σ_{u0} is the shape parameter of the GPD for excesses over threshold μ_0. From eq.(34), $E[X-\mu|X>\mu]$ is a linear function of μ, which yields a graphical identification for appropriate threshold in modelling extreme values via the GPD. The above tools comprehensively dealt with the stability, flatness and linearity. For the interpretation subject to threshold selection, the POT package implemented in R was used [39].

III. Eshelby's Inclusion Problem

3.1 Introduction

Eshelby's problem [8, 40] for the elastic fields in an ellipsoidal inclusion embedded within an infinite matrix is used as a benchmark to verify the TE-FEM and TE-FFT prediction. The well-known explicit formulae were derived by Eshelby that involve the elegant tensor named Eshelby tensor which links the strain in an inclusion to the eigenstrain. With this, elastic stress and strain fields inside the inclusion appeared to have uniform and homogeneous distribution. In micromechanics of materials, this solution has been cornerstone to estimate the effective properties, especially for the matrix-inclusion composites [41, 42]. The comprehensive description concerning Eshelby's problem can be found in the book of Mura [43].

Recently, B.S. Anglin *et al*. [20] used the Eshelby's analytical solution for spherical and cylindrical inclusion geometries to verify the numerical method based on the FFT. It was found that the micromechanical behavior for simple geometries, i.e. spherical and cylindrical inclusion configurations, are in reasonably good agreement with the analytical solutions of the Eshelby. With reference to this well demonstrated results, spherical homogeneous inclusion configuration is adopted to verify two simulation methods as well as to investigate the discrepancy between two methods in predicting thermoelasticity.

3.2 Simulation parameters

We began by assuming the isotropic elasticity for the composite of matrix-inclusion type. Material properties were determined refer to the previous work of B.S. Anglin et al [20] where the effect of stress in whisker formation of β-tin is considered. The relevant stiffness tensor of inclusion and matrix were calculated from isotropic elastic properties of β-tin (Young's modulus and Poisson's ratio are 65.4GPa and 0.42, respectively). The CTE tensor of inclusion and matrix was also calculated from the coefficients of linear thermal expansion, which are 15×10^{-6} and 10×10^{-6} for inclusion and matrix, respectively. Thermal loading of 1000 K is applied to impose temperature gradient, thereby producing misfit strain of 0.005 between inclusion and matrix.

Input microstructures with spherical inclusion (red) embedded in an infinite matrix (white in left, gray in right) are discretized on a regular voxel grid as shown in Fig.2. To investigate the effect of

ULSAN NATIONAL INSTITUTE OF SCIENCE AND TECHNOLOGY

resolution on thermoelastic simulation, microstructure with size (a),(b) 32×32×32 and (c),(d) 64×64×64 are generated, where the left figures represent three-dimensional views, and, right figures show its corresponding cross-sectional views. Here, a volume fraction of spherical inclusion is maintained as 0.8%, so the radius of voxelized sphere is roughly determined to be 4 and 8 voxel elements for dimension 32×32×32 and 64×64×64. The structural elements of eight-node linear 3D brick element with one Gauss points (C3D8R) are used for the FEM-based simulation, corresponding to a periodic unit cell of the one-point FFT-based simulations.

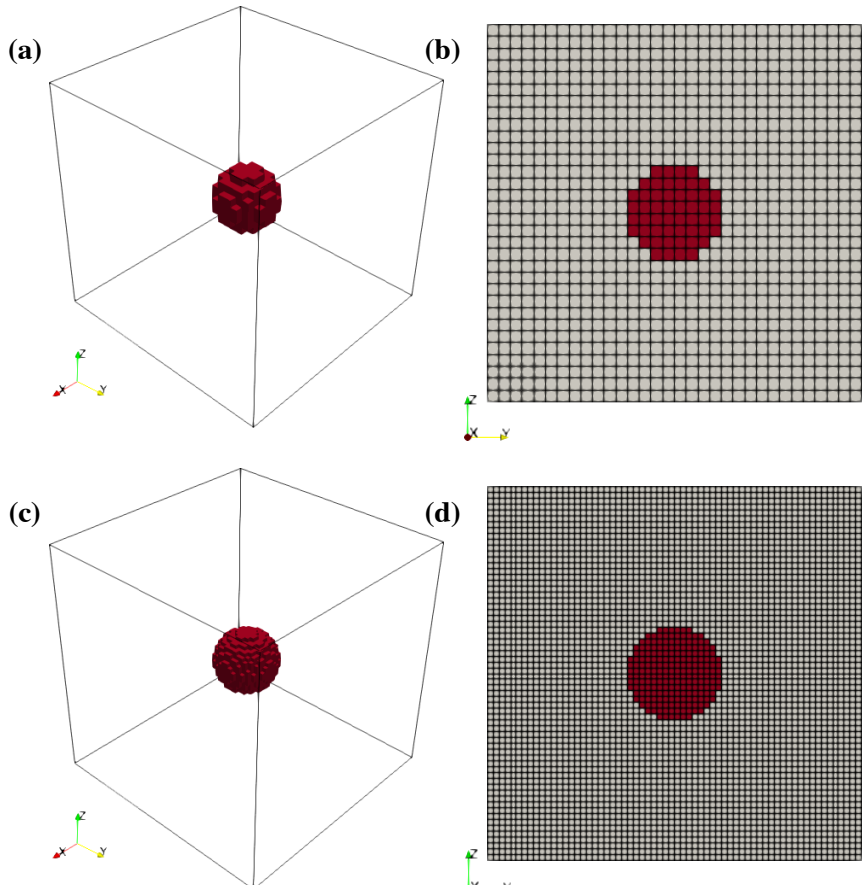

Figure 2. 3D digital microstructure with spherical inclusion (red) embedded in an infinite matrix is discretized on a regular voxel grid (a),(b) 32×32×32 and (c),(d) 64×64×64.

3.3 Results & Discussion

As a result of simulation for the Eshelby problem, stress distribution, especially diagonal components (σ_{11}, σ_{22}) of the stress tensor were used for visualization and analysis of the results. The profile of each distribution was also compared to the Eshelby's analytical solution line to verify both simulation methods.

3.3.1. Stress distribution

Stress distribution on the cross section (the section in the middle of z-axis with x-axis horizontal, y-axis vertical) predicted from TE-FEM and TE-FFT are shown in Figs.3 and 4, where Fig.3 shows the results corresponding to the microstructure with size 32×32×32 and fig.4 shows its higher resolution, with size 64×64×64. In both Figs 3 and 4, σ_{11} distribution resulting from (a) TE-FEM and (b) TE-FFT are represented, and, differences between two methods, defined by results of TE-FFT subtracted from TE-FEM, are depicted in (c). Corresponding results of σ_{22} are depicted in (d)-(f) in the same manner. Both predictions indicate a similar trend that diagonal stress values (σ_{11} and σ_{22}) approach zero at the edges, demonstrating that periodic boundary conditions of input microstructure are well applied in terms of infinite matrix of Eshelby's case. In Fig.3, each diagonal stress predicted from (a), (d) TE-FEM shows large oscillation like mosaic pattern, especially near inclusion-matrix interfaces, while (b), (d) TE-FFT represents monotonically changing distribution. The differences between two methods are presented in (c) and (f). The region where TE-FEM calculates higher stress than TE-FFT is expressed as red while its opposite case is represented as blue. Such differences also appeared as mosaic pattern at local interfaces, which may be affected by TE-FEM prediction. It is also found that the variations observed in TE-FEM prediction mitigated with increasing resolution from 32×32×32 to 64×64×64 as shown in Fig.3 (a), (d) and Fig.4 (a), (d). Moreover, local differences between each calculation also decreased with increasing resolution.

3.3.2 Stress profiles

In order to verify the elastic response calculated from each method, σ_{11} and σ_{22} components along x-axis through the center of the microstructure were measured and compared to the Eshelby's analytical solution. The corresponding stress profile for 32×32×32 and 64×64×64 resolutions are shown in Figs.5 and 6, respectively. As has previously been explained, stress values are observed to be closer to zero as the distance from the center of microstructure approaches to both edges. Stress profiles predicted from TE-FEM and TE-FFT for 32×32×32 resolution is overlaid on calculated Eshelby's stress profile (black solid line), respectively. Here, stress value resulting from TE-FEM is represented as red open square, and of TE-FFT is depicted as blue open circle. It is notable that in both Figs.5 and 6, (a) σ_{11} and (b) σ_{22} profiles follow the Eshelby's analytical line roughly, while most of deviations are observed near inclusion-matrix interfaces as shown in magnified graph in the right of each figure.

According to the Eshelby's solution, theoretical homogeneous stress inside the inclusion is -376.05 MPa and corresponding average σ_{11} predicted from TE-FEM and TE-FFT are -370.99 and -375.93 MPa, respectively. The relative differences between Eshelby and each method is 1.35% for TE-FEM prediction and 0.03% for TE-FFT prediction. It implies that prediction of TE-FFT is much closer to the analytical solution of Eshelby.

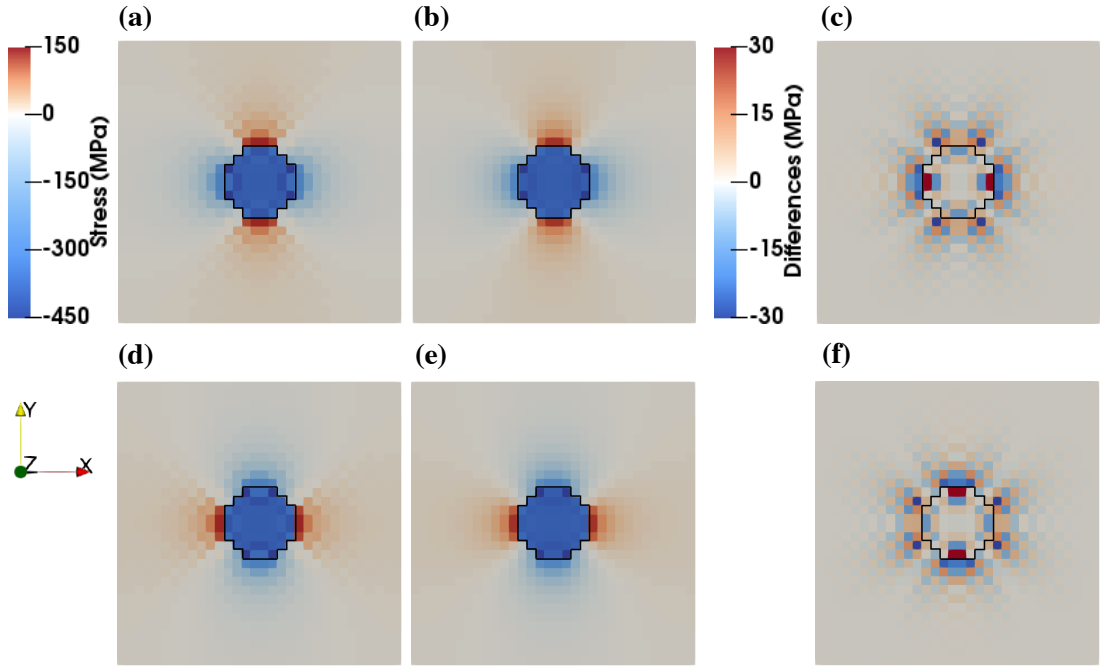

Figure 3. Stress fields on cross section (the section in the middle of z-axis with x-axis horizontal, y-axis vertical) predicted by TE-FEM and TE-FFT for a 32×32×32 resolution. σ_{11} distribution resulting from (a) TE-FEM, (b) TE-FFT, and (c) differences between each method are shown. (d)-(e) are corresponding distribution of σ_{22}.

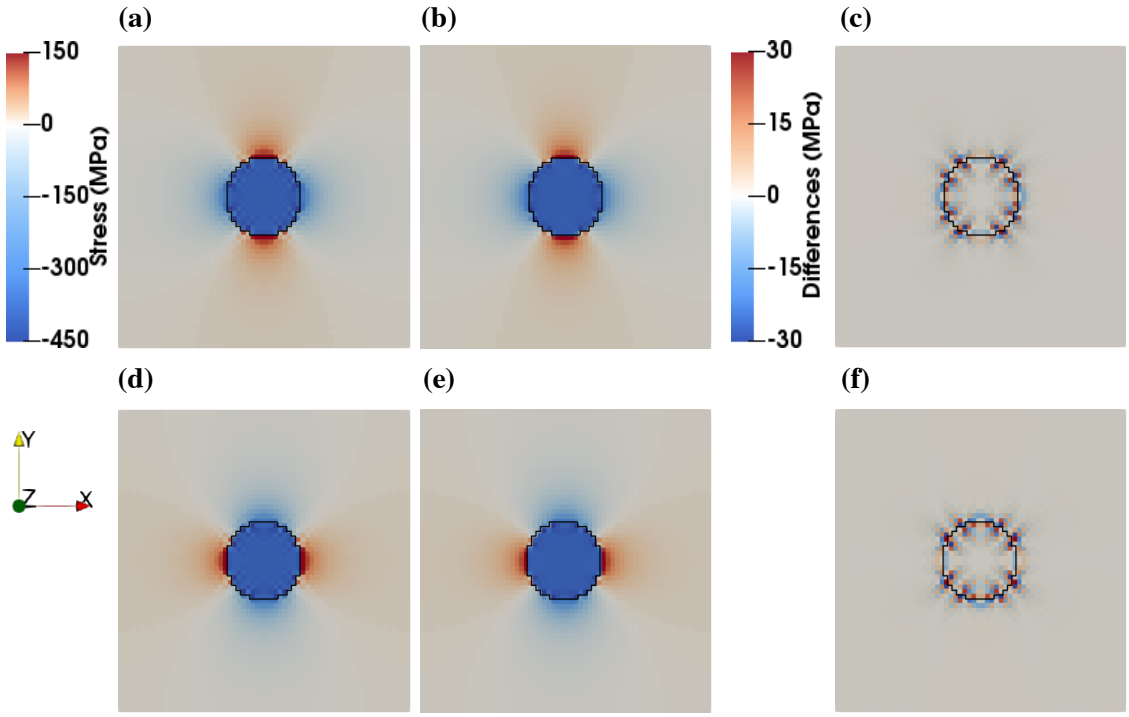

Figure 4. Stress fields on cross section predicted with TE-FEM and TE-FFT for a 64×64×64 resolution. σ_{11} distribution resulting from (a) TE-FEM, (b) TE-FFT, and (c) differences between each method are shown. (d)-(e) are corresponding distribution of σ_{22}.

ULSAN NATIONAL INSTITUTE OF SCIENCE AND TECHNOLOGY

In Fig.5 (a), σ_{11} profile calculated from TE-FFT shows comparatively monotonic distribution as observed in previous section while a certain amount of fluctuation is observed in TE-FEM prediction. (b) Average σ_{22} inside the inclusion computed from TE-FEM and TE-FFT are -373.08 and -371.01 MPa, respectively. As with σ_{11} profile, TE-FEM prediction shows relatively severe variation than TE-FFT prediction in calculating σ_{22} profile. Similarly, each stress profile for 64×64×64 resolution is presented in Fig.6. It is observed that variations performed in $32\times32\times32$ resolution became weaker with increasing resolution, which implies that 64×64×64 resolution is much reasonable to approximate Eshelby's solution. Average and standard deviation of stress within the inclusion depending on each resolution is given in Table 1. It is also found that the difference and standard deviation with respect to Eshelby's analytical solution were decreased with refined, higher resolution.

In terms of computation time, FFT-based simulation for a homogeneous Eshelby case with size 32×32×32 and 64×64×64 only took less than a minute in apple iMac (3.2GHz quad-core Intel Core i5). In the meantime, for an FEM simulation, a dual core processor desktop machine (Intel Xeon 2.3 GHz CPU) is used. 232sec. and 2,103sec. was required to implement Eshelby's case with resolution 32×32×32 and 64×64×64, respectively, as shown in Table 2.

Table 1.
The average and standard deviation of σ_{11} and σ_{22} distribution inside the inclusion. The analytical value measured by Eshelby's theory is 376.05 MPa

Resolution	Analytical value	Average (Standard deviation)			
		σ_{11} (MPa)		σ_{22} (MPa)	
		FEM	FFT	FEM	FFT
32×32×32	-376.05	-370.99 (24.45)	-375.93 (7.74)	-373.08 (10.40)	-371.01 (3.88)
64×64×64		-372.92 (7.10)	-373.81 (5.10)	-372.26 (4.02)	-372.21 (2.55)

Table 2.
The simulation time for computing Eshelby problem.

Resolution	Computation Time (sec.)	
	FEM	FFT
32×32×32	232	2
64×64×64	2,103	17

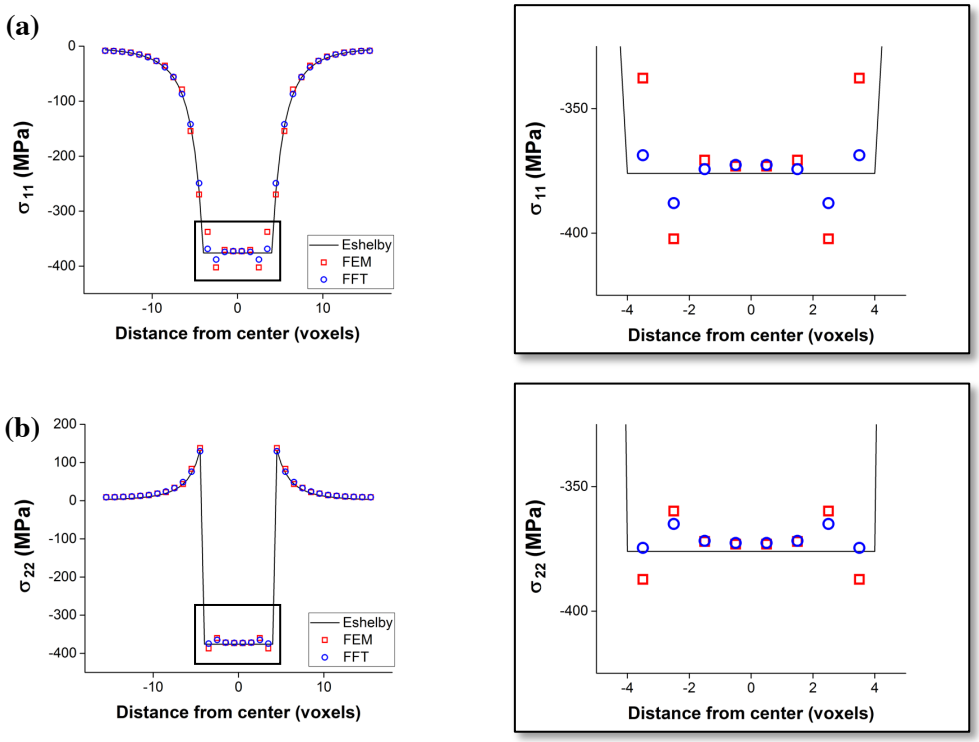

Figure 5. Profiles resulting from TE-FEM (red open circle) and TE-FFT (blue open circle) for 32×32×32 resolution on stress profile calculated from Eshelby (black solid line).

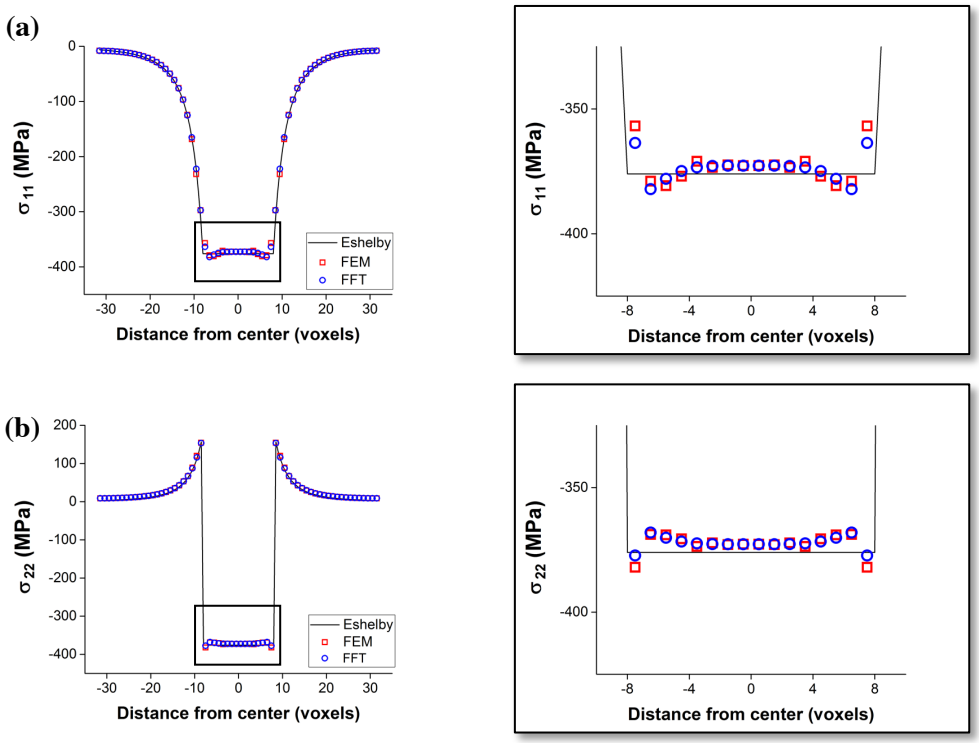

Figure 6. Profiles resulting from TE-FEM (red open circle) and TE-FFT (blue open circle) for 64×64×64 resolution on stress profile calculated from Eshelby (black solid line).

IV. Thermoelastic Response of a Polycrystalline Material

4.1 Introduction

In order to investigate the elastic local fields of polycrystalline material under thermal loading, a voxellated, three-dimensional hypothetical polycrystal is generated as an input microstructure. In this study, materials with isotropic and anisotropic case were considered. For the simulation of isotropic case, material properties of Al7075, having FCC crystal structure, were used to examine the elastic response resulting from isotropic CTE and anisotropic nature of stiffness tensor. For the anisotropic case, material properties of Ti-5Al-2.5Sn α-Ti alloy were used to analyze the effect of anisotropy in stiffness and CTE tensor.

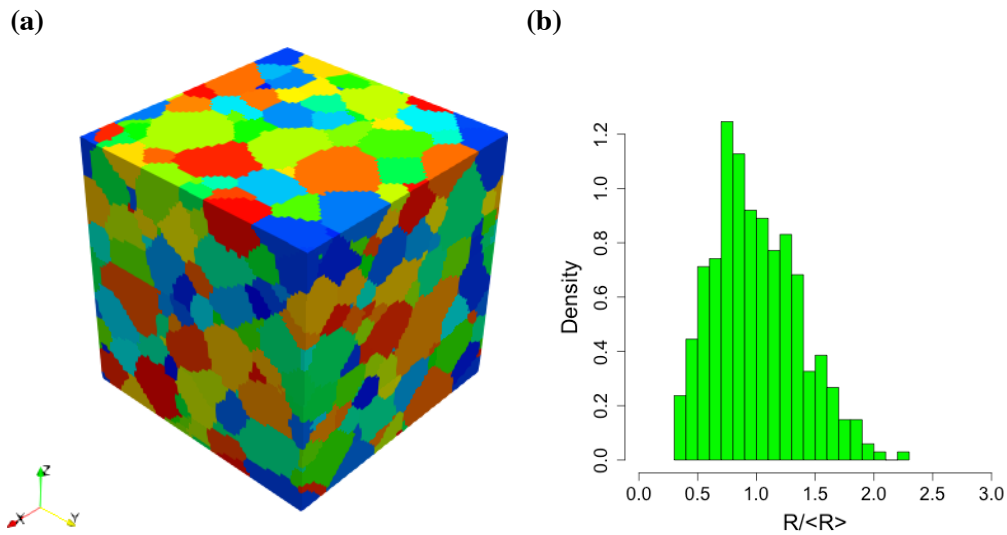

Figure 7. (a) A generated hypothetical 3D microstructure with size 64×64×64 and (b) its corresponding normalized grain size distribution.

4.2 Model description

As an input microstructure (RVE) for TE-FEM and TE-FFT simulations, a 3D hypothetical polycrystalline microstructure was generated by means of Monte Carlo grain growth method. The process of grain growth was carried out while being forced to have a periodic grain structure in every three direction, so that the periodic boundary conditions for the FEM and FFT simulations could be optimized. Fig.7 shows (a) the generated hypothetical microstructure and (b) corresponding distribution of normalized grain size, with respect to the radius of grain. Dimension of the synthetic microstructure was 64×64×64 and average grain radius distributed in the microstructure was 5.06. As shown in Fig.8 (b), grain size does not exhibit in small value (< 0.3), implying that grains with small size were

ULSAN NATIONAL INSTITUTE OF SCIENCE AND TECHNOLOGY

purposely removed to avoid complexity of elements for simulation, due to the small element size with different orientation. The generated polycrystalline microstructure consists of 337 grains, and, individual color scale in Fig.7 (a) indicates that different orientation (spin number) is assigned to each grain.

Both the isotropic and anisotropic case were taken into account to investigate the discrepancy in elastic response between TE-FEM and TE-FFT predictions as well as to explore the effects of isotropy and anisotropy on thermoelastic response of polycrystal according to the simulation methods. In order to impose thermal loading, temperature of the system was increased from 0K through 300K for both simulations.

4.3 Isotropic Case

4.3.1 Material Selection

For the isotropic case, material properties of Al7075 is used. Both the effect of texture and anisotropic nature of cubic material are assured by assigning relevant tensor to corresponding grains, which are rotated beforehand on the basis of their crystallographic orientations. In this regard, 5 sets of random orientations are generated, and, used to compensate the influence of randomness. The elastic stiffness coefficients used for the simulations are as follows, which are calculated from the young's modulus and Poisson's ratio of Al7075 given in Refs [44].

$$C_{11} = 105.2GPa,\ C_{12} = 51.8GPa,\ C_{44} = 26.9GPa \tag{35}$$

The CTE tensors are in accordance with the linear CTE given by:

$$\alpha_{11},\ \alpha_{22},\ \alpha_{33} = 21.6\cdot 10^{-6}/\mathrm{K} \tag{36}$$

4.3.2 Comparison of local response: von Mises equivalent stress distribution

In this section, the field variable used is von Mises equivalent stress and is referred to as 'stress' without further qualification. In Fig.8, stress distribution on the exterior surfaces of the microstructure is visualized where (a) represents results from TE-FEM approach for orientation set 1 to 5, respectively, and (b) displays corresponding results from TE-FFT approach. The high level of stress is indicated as red, while low level is represented as blue. The pattern in stress distribution resulting from both methods are visually consistent, where high stress is appeared in the grain boundaries, which implies that the variations in stress are affected by the grain structure.

Fig.9 (a) shows calculated differences (Subtraction of TE-FFT prediction from TE-FEM prediction) in stress between two predictions. When TE-FEM prediction is higher than TEFFT

ULSAN NATIONAL INSTITUTE OF SCIENCE AND TECHNOLOGY

prediction, stress field is identified as red, and, represented as blue for the opposite case. A few differences between two predictions are depicted as green in the spectrum. Large differences are observed in the grain boundaries, junctions, and small grains, consistent with the characteristic of localized high stress. Fig.9 (b) shows corresponding percent error which are calculated from absolute value of differences divided by stress values from FFT prediction multiplied by 100. The distributions of estimated percent error again display similar trend that observed in differences, as in (a). It is inferred that such behavior is involved in extreme values of high stress (hot spots) other than average value of stress.

To observe the relationship between stress distribution and grain structure, plots of stress versus grain size (i.e. normalized radius of grain) are derived as shown in Fig.10. Here, the microstructure with orientation set 1 is used as a representative. (a) In the scatter plot, results from both methods yield similar response that stress values are inversely proportional to the grain size. (b) In box plot, data sets with respect to the normalized grain size are divided into 0.5 and displayed with error bar (i.e. standard deviation). These results indicated a more definite conclusion that average and standard deviation of stress are increased with decreasing grain size. In both plots, results from TE-FEM and TE-FFT were indicated as red and blue symbols, respectively. In addition, the ratio of stress resulting from two methods (stress from TEFEM / stress from TEFFT) versus grain size is compared as shown in Fig.11, where (a) shows the plot with wider range of stress ratio (from 0 to 1.2) and (b) limited its stress range as from 0.96 to 1.06 so as to obtain more precise information. The variations in the stress ratio (i.e. differences in calculated stress between TE-FEM and TE-FFT) are observed to have relatively wider range (0.975 ~ 1.05) in small grains, while it is narrow, approximately 1.0 in large grains (at the right end point in the plot).

In what follows, probability density functions of stress resulting from TE-FEM and TE-FFT for 1 to 5 sets of test microstructure are overlaid as shown in Fig.12. The histogram of stress data sets calculated from TE-FEM and TE-FFT is represented as red and blue, respectively. However, it is hard to distinguish the distinctiveness between each result due to the strong resemblance in both distributions. Otherwise, these graphs can be indicative of normal shape and long upper tails of distributions, consistent with the appearance of hot spots shown in Fig.9.

Table 3. summarizes the descriptive statistics for stress for all five sets of test microstructure. It is notable that average, maximum, and standard deviation of stress resulting from TE-FEM is higher than TE-FFT for every five case, denoting the potential distinction between two methods are engaged in extreme values of the stress distribution.

ULSAN NATIONAL INSTITUTE OF
SCIENCE AND TECHNOLOGY

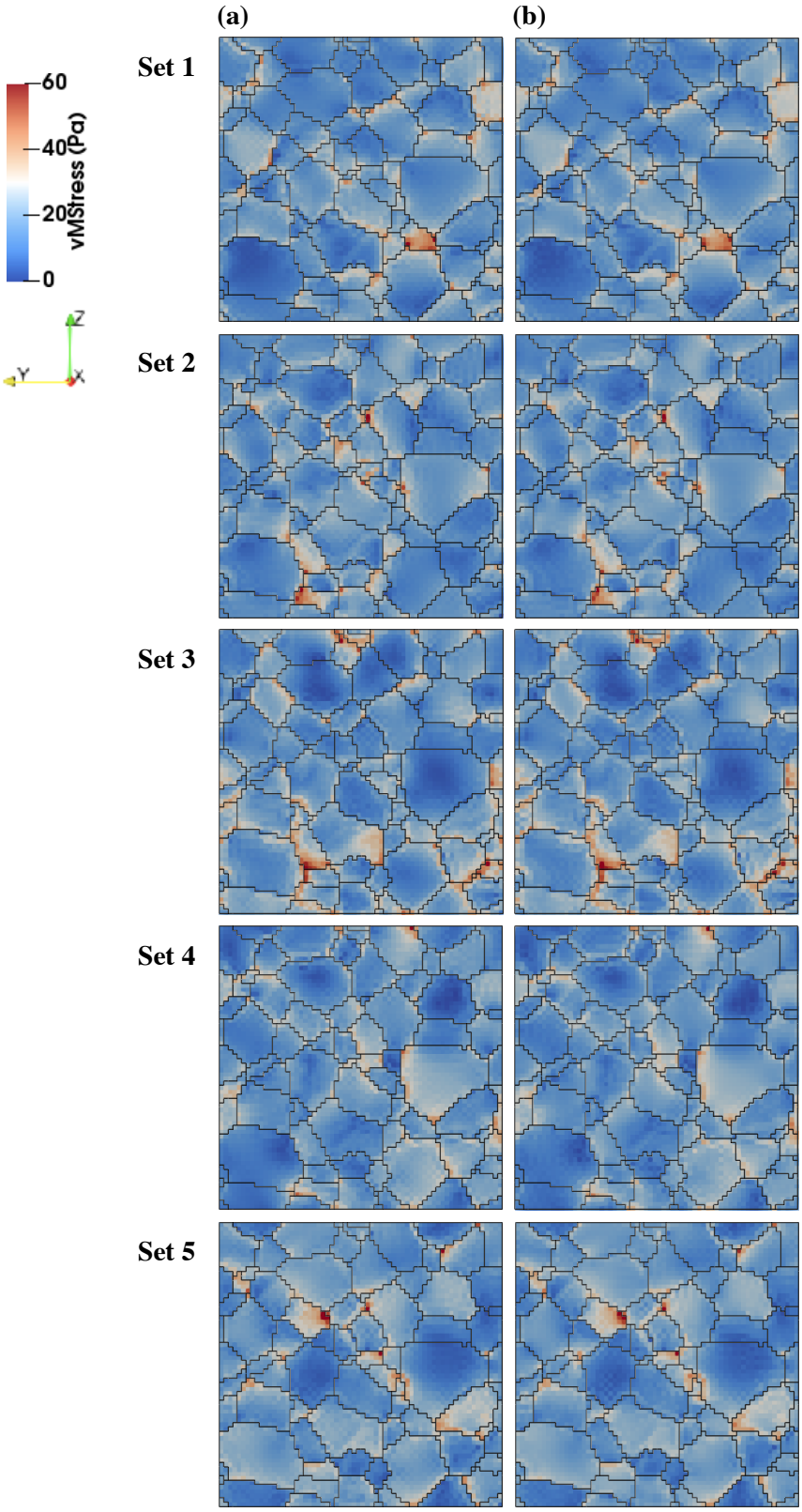

Figure 8. Stress field (von Mises equivalent stress) on the cross section of the microstructure. (a) prediction from TE-FEM for random orientation set 1 to 5, respectively, and (b) displays relative results from TE-FFT.

ULSAN NATIONAL INSTITUTE OF
SCIENCE AND TECHNOLOGY

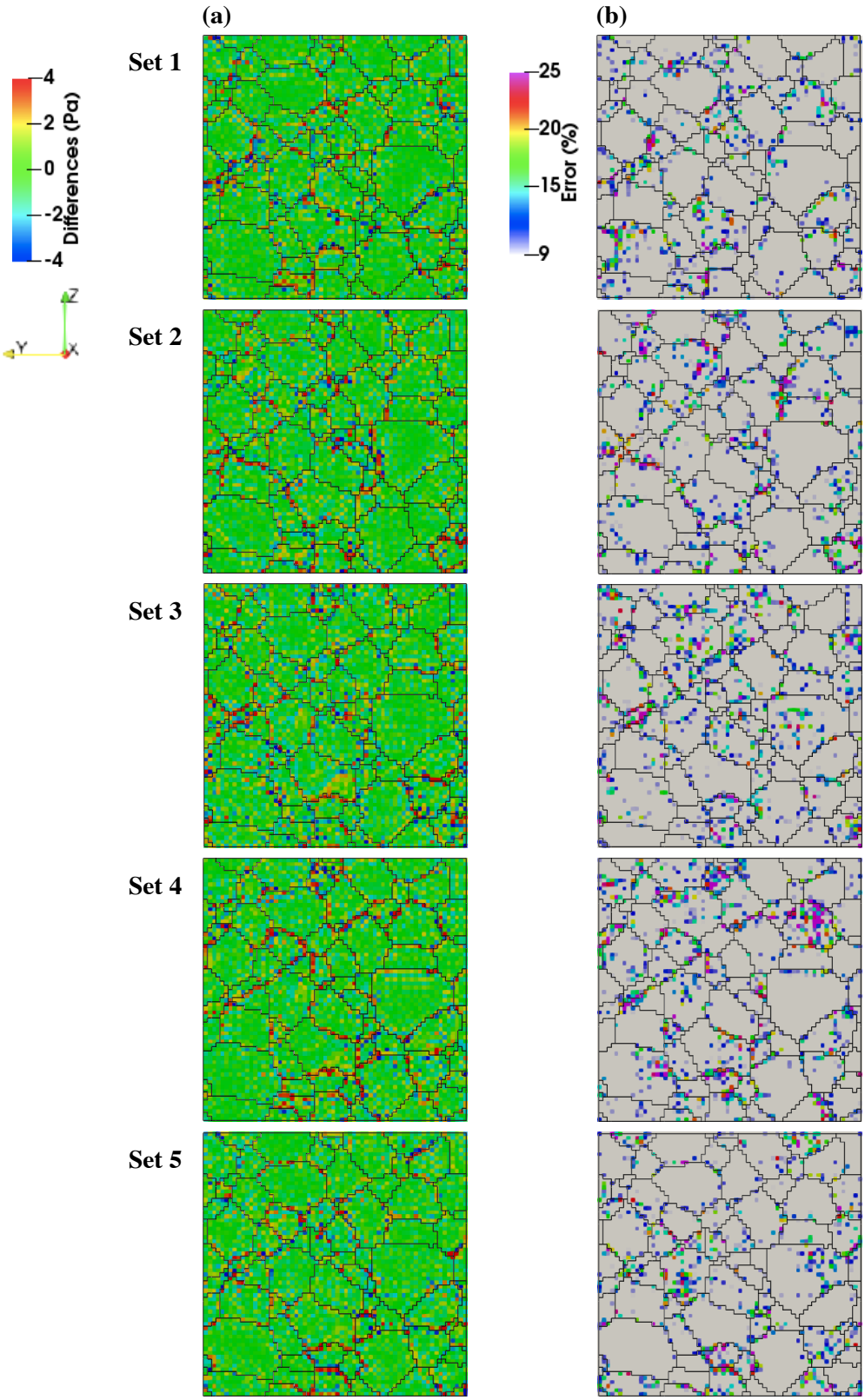

Figure 9. (a) Calculated differences in stress between two methods. When TEFEM prediction is higher than TEFFT prediction, stress field is identified as red, and, represented as blue for the opposite case. (b) Percent error calculated from absolute value of differences divided by stress values from FFT prediction times 100.

ULSAN NATIONAL INSTITUTE OF SCIENCE AND TECHNOLOGY

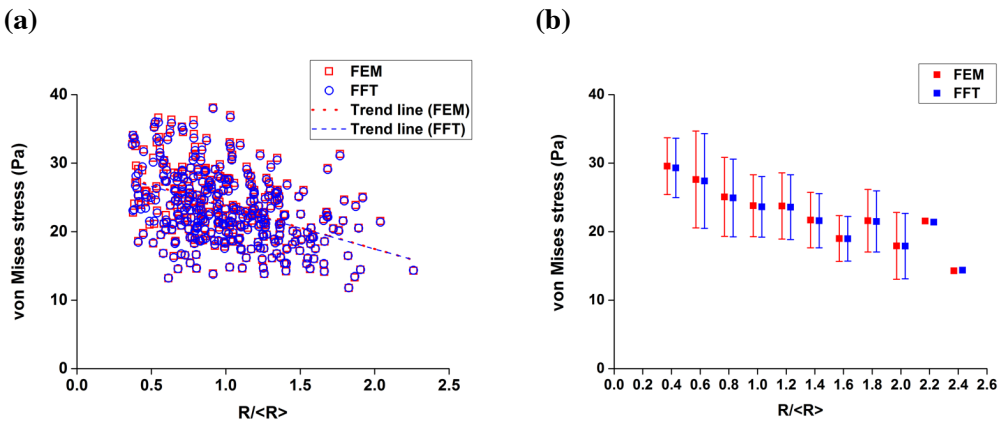

Figure 10. (a) Scatter plot and (b) box plot of stress versus normalized grain size

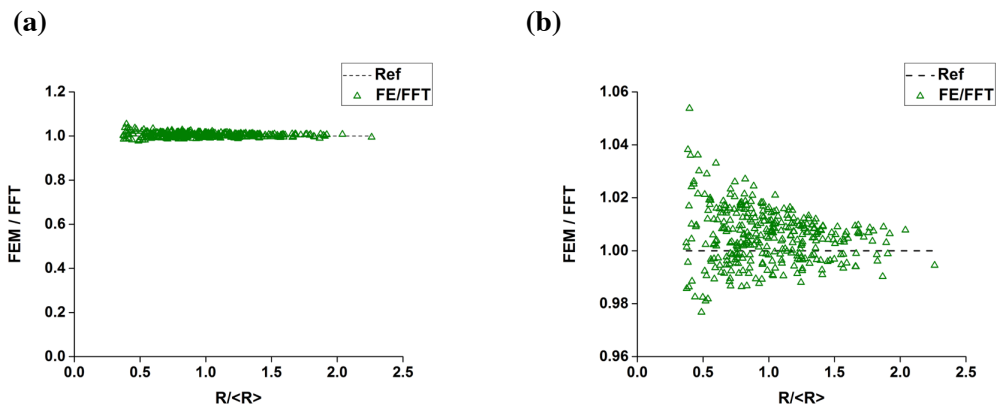

Figure 11. The ratio of stress resulting from two methods versus grain size

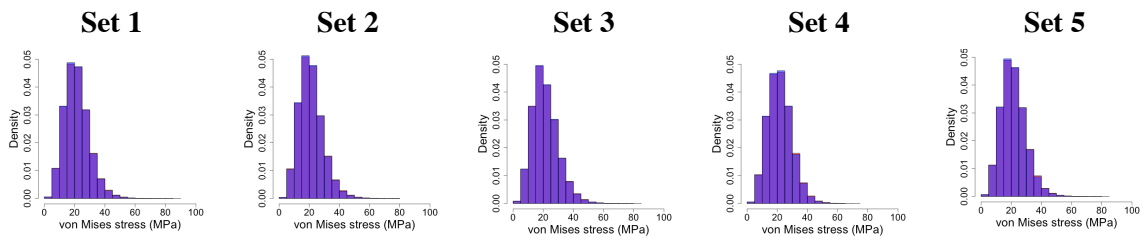

Figure 12. Probability density functions for stress resulting from TE-FEM (red) and TE-FFT (blue)

Table 3.
Descrptive statistics for stress for all five sets of test microstructure for isotropic case.

	Set 1		Set 2		Set 3		Set 4		Set 5	
	FEM	FFT	FEM	FFT	FEM	FFT	FEM	FFT	FEM	FFT
Mean	21.50	21.40	21.25	21.16	21.36	21.28	21.74	21.63	21.54	21.43
Min.	1.13	1.10	1.19	1.28	1.59	1.57	1.32	1.08	1.75	1.44
Max.	85.79	80.74	78.51	77.35	82.21	79.27	73.98	64.33	82.12	77.54
Std.dev.	8.20	8.05	8.08	7.94	8.56	8.42	8.00	7.85	8.23	8.09

4.3.3 Statistical Extreme Value Techniques

In order to quantitatively compare the extremely high stress between TE-FEM and TE-FFT in terms of upper tail in distribution, extreme value analysis is applied [45]. In this case, probability plot is useful for testing lognormality of data set, depicting straight diagonal line if the data converges to truly lognormal distribution [46]. In this section, stress values of all five test microstructures have been combined into one data set for a comprehensive analysis, and, each value is normalized by its means for the direct comparison and quantification.

Probability plots of comprehensive stress data sets resulting from both methods are plotted on the same graph as shown in Fig.13, where red open circle represents the stress from TE-FEM prediction and blue open circle indicates stress from TE-FFT prediction. A reference line is based on the theoretical probabilities estimated from both predictions. As mentioned above, a data close to unit diagonal implies reasonable model for lognormal distribution. In the meantime, substantial tail departures from linearity were appeared in both results.

The upper tails of data sets from two methods were analyzed using extreme value tail fitting. Fig.14 shows the threshold choice plots and mean residual life plots for the data sets from (a) TE-FEM prediction and (b) TE-FFT prediction, respectively. As explained above, appropriate threshold calls were determined, subject to the stability and flatness of data plots (i.e., modified scale and shape parameters are constant above threshold call, once the GPD approximates an adequate tail). Therefore, appropriate threshold call could be selected in the range of 1.4 to 1.6 in both results. In terms of mean residual plot, graph is known to became linear above threshold level. In mean residual plots for both approaches, there is some evidence for linearity above 1.5. However, as the interpretation of threshold choice plot and mean residual life plot is not simple, POT package implemented in R is used to select threshold [39]. Statistics containing threshold call and the number of points above threshold call for the selected data sets of stress distribution are shown in Table 3. In this work, selected threshold calls are same for both methods, but, data sets from TE-FEM prediction appeared to have relatively large exceedances than from TE-FFT prediction.

In what follows, the exceedances above threshold, i.e., the upper tails of the distribution were fitted to the GPD. For implementing fitting procedure, we also used POT packages in R. Scale (σ) and shape (ξ) parameters were found to be 0.26836, -0.03446 for TE-FEM predictions and 0.26009, -0.04899 for TE-FFT prediction, respectively. Resulting diagnostic plots for the fitted GPD are shown in Fig.15. As discussed in section 2.4, scale parameter denotes the spread of the fitted GPD while shape parameter governs length of the GPD tail. As the TE-FEM data set had larger scale parameter than the (a) TE-FFT data sets, indicating larger spread. As smaller shape parameter indicates a shorter tail, (b) TE-FFT has much shorter tail than TE-FEM. By quantifying spread and length of the GPD tail based on the parameters, distinctiveness between two methods could be stated that TE-FEM predicts much higher hot spots (extreme values) than TE-FFT as well as bring out much more hot spots.

ULSAN NATIONAL INSTITUTE OF SCIENCE AND TECHNOLOGY

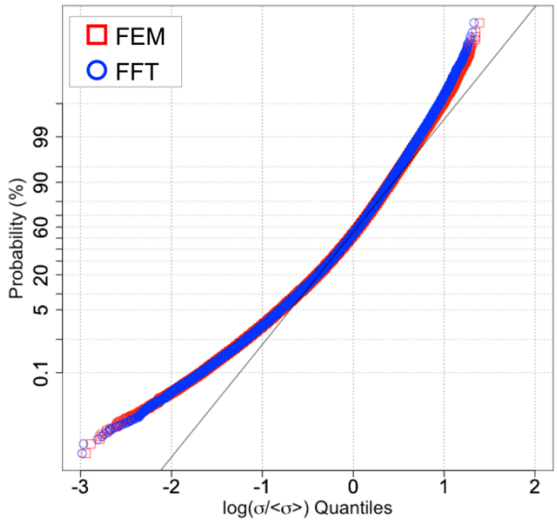

Figure 11. Probability plots of normalized stress resulting from TE-FEM (red) and TE-FFT (blue)

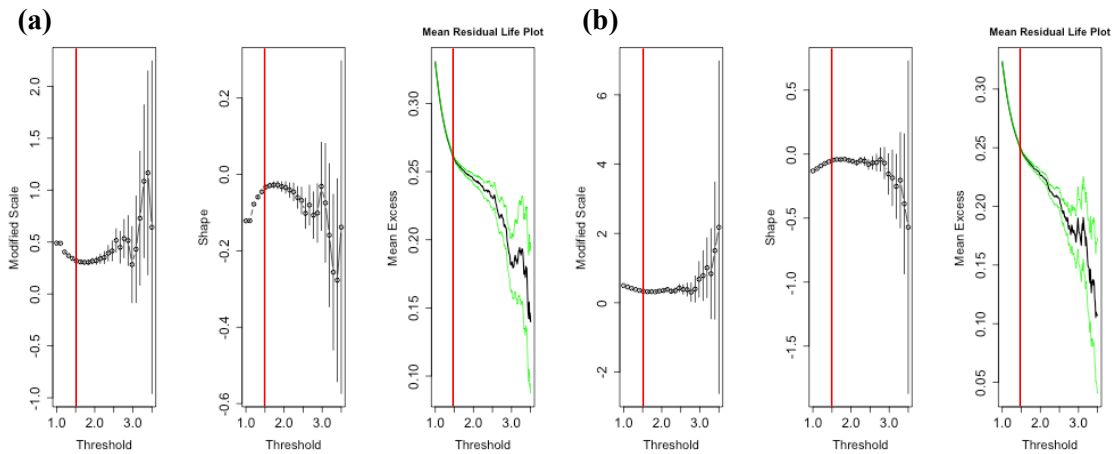

Figure 12. Threshold choice plots and mean residual life plots for the stress resulting from (a) TE-FEM and TE-FFT.

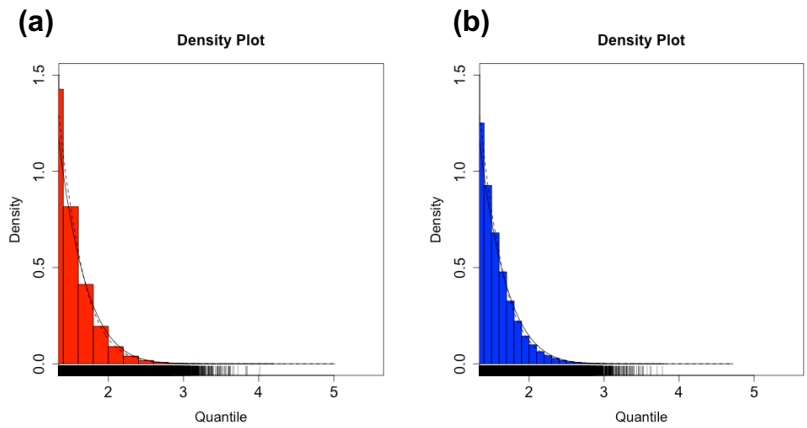

Figure 13. Diagnostic plots for the fitted GPD

ULSAN NATIONAL INSTITUTE OF SCIENCE AND TECHNOLOGY

Table 4.
Statistics for the stress data sets from TE-FEM and TE-FFT

	Points above threshold (Proportion)	**Threshold call**
TE-FEM	134,355 (0.1025)	1.5
TE-FFT	128,847 (0.0983)	1.5

4.4 Anisotropic Case

4.4.1 Material Selection

To examine the influence of the anisotropy on thermoelasticity, material properties of α-Ti alloy with hcp crystal structure were applied owing to its inherent anisotropy in stiffness and CTE. The coefficients of elastic stiffness are as follows, which are obtained from the literature [47].

$$C_{11} = 160GPa, \quad C_{12} = 90GPa, \quad C_{33} = 181GPa, \\ C_{44} = 46.5GPa, \quad C_{66} = 35GPa \tag{35}$$

CTE is significantly dependent on temperature, and highly correlated with crystallographic orientations. Contrary to the isotropic case of Al alloy, two principal axial coefficients are necessary to discuss the thermal expansion of anisotropic material. The CTE of α-Ti alloy were found to be [47]:

$$\alpha_{11}, \alpha_{22} = 17.8 \text{ and } \alpha_{33} = 10.4 \tag{36}$$

By using eq.(3), the calculated anisotropy ratio in α-Ti alloy was 0.58, represents its high level of thermal expansion anisotropy.

4.4.2 von Mises equivalent stress distribution

Anisotropic material properties of α-Ti alloy are rotated by random orientation sets 1 to 5, and, assigned to individual grains. Stress distribution on the microstructure were visualized in Fig.16. Like as Isotropic case, high stresses are locally distributed in the grain boundaries. By the way, on the contrary to the isotropic case, remarkable differences between each method are observed, especially in grain boundaries and small grains. Fig.17 shows (a) difference and (b) error percent distributions, which allows a more significant assessment of the distinctiveness between two methods. Since same hypothetical microstructure was used for simulation of both the isotropic and anisotropic cases, the only difference in input is material properties. Therefore, it can be concluded that anisotropy of materials affects the thermoelastic response of each method. Indeed, heterogeneous stiffness tensor and CTE give rise to inhomogeneous stress distribution near boundaries, and such responses are appeared to be

ULSAN NATIONAL INSTITUTE OF SCIENCE AND TECHNOLOGY

different depending on the simulation methods. With respect to the maximum error percent, result of anisotropic case shows much higher maximum error percent than isotropic case.

Probability density function for TE-FEM and TE-FFT calculations with 1 to 5 set is represented in Fig.19. Again, in contrast with isotropic case, different trend of distribution is clearly verified in mean and shape of each distribution. Moreover, as shown in descriptive statistics summarized in Table 4, the average, maximum, and standard deviation of stress resulting from TE-FFT were larger than TE-FEM. It is inferred that anisotropic behavior can be influenced by the calculation methods, where FEM adopted local equilibrium and FFT applied full field equilibrium.

4.4.3 Application of Eshelby problem to anisotropic case

During verification process using Eshelby's solution, only isotropic case was considered. Here, in order to figure out the discrepancy between isotropic and anisotropic case, the Eshelby problem is applied for the simulations of anisotropic case. At this time, von Mises equivalent stress was investigated for an analysis, consistent with the thermoelastic analysis of polycrystalline microstructure.

Isotropic material properties of β-tin is applied and its stress (von Mises equivalents tress) distribution is analyzed for a direct comparison. As shown in Fig.19, orientation of inclusion is rotated by Bunge Euler angle, increasing 30 degree from 0 to 90 degree. In (a)~(d), left two figures represent stress fields in cross-section resulting from TE-FEM and TE-FFT. Despite it was hard to distinguish differences between each method in terms of diagonal stress in section 3.3.1, notable variations are appeared inside the inclusion and near the interface, in terms of von Mises equivalent stress. Meanwhile, stress profiles resulting from both methods approximately follow the Eshelby's analytical line as shown in the right. By the way, no particular trend was observed according to the changing rotation.

As an anisotropic material property, α-Ti alloy is selected and the orientation of inclusion is also rotated. Stress distributions and profiles with changing orientation are shown in Fig.20. (a) Before the rotation (i.e., the orientation angle set of inclusion is 0°, 0°, 0°), deviation is not large. When (b) the x-axis angle is rotated from 0° to 30° (i.e., the orientation angle set of inclusion is 0°, 30°, 0°), stress inside the inclusion predicted from TE-FFT is significantly increased relative to the TE-FEM prediction. In this case, both stress distribution and profile show significant differences between two responses. Such tendency is still noticeable when (c) the x-axis angle is rotated from 30° to 60°. Consequently, it is assumed that TE-FEM approach is less sensitive to anisotropic effect than TE-FFT approach. In other words, the sensitivity to anisotropy is different according to the simulation methods.

ULSAN NATIONAL INSTITUTE OF
SCIENCE AND TECHNOLOGY

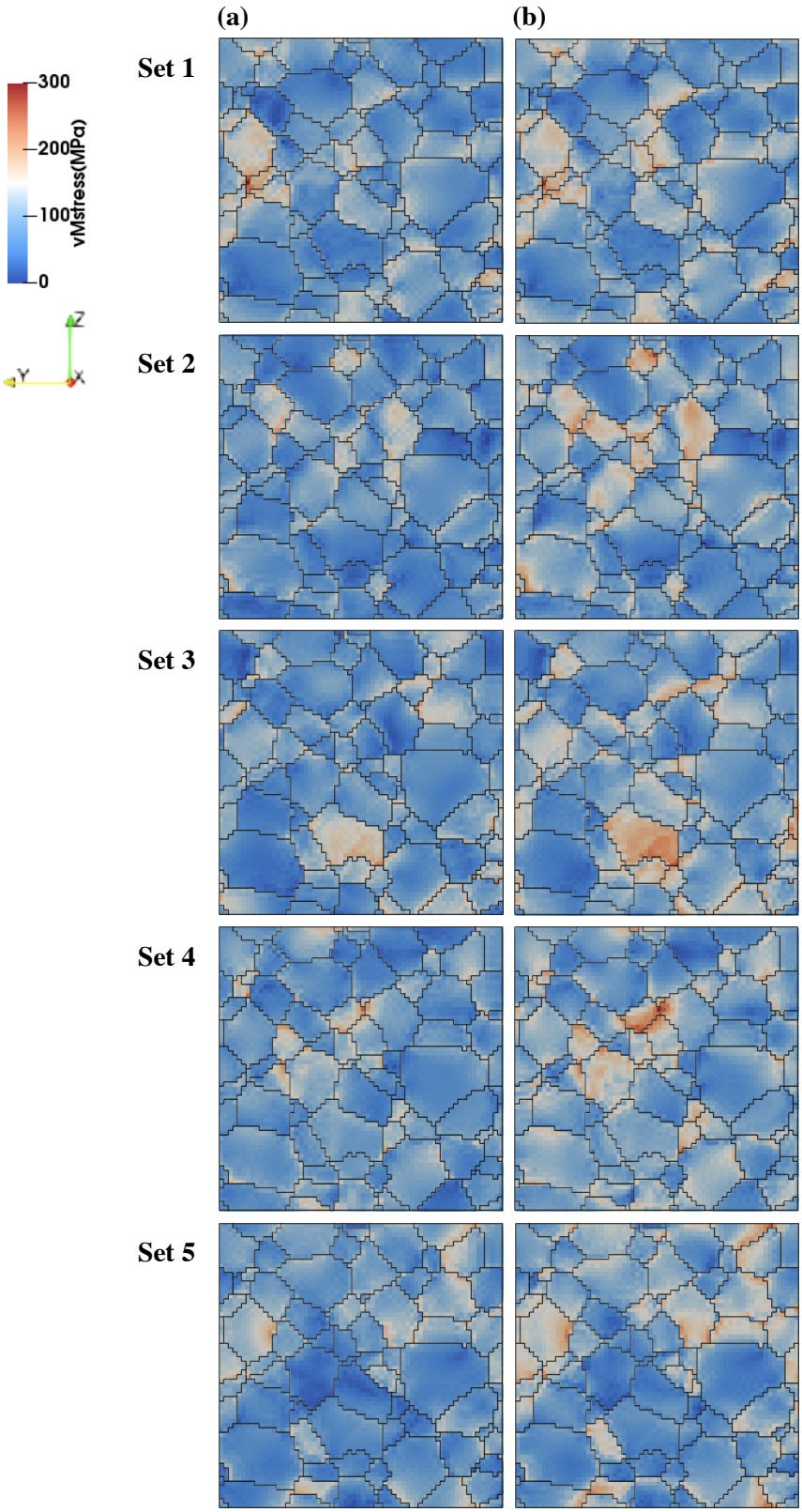

Figure 14. Stress fields on the cross section of the microstructure. (a) prediction from TE-FEM for random orientation set 1 to 5, respectively, and (b) displays relative results from TE-FFT.

ULSAN NATIONAL INSTITUTE OF
SCIENCE AND TECHNOLOGY

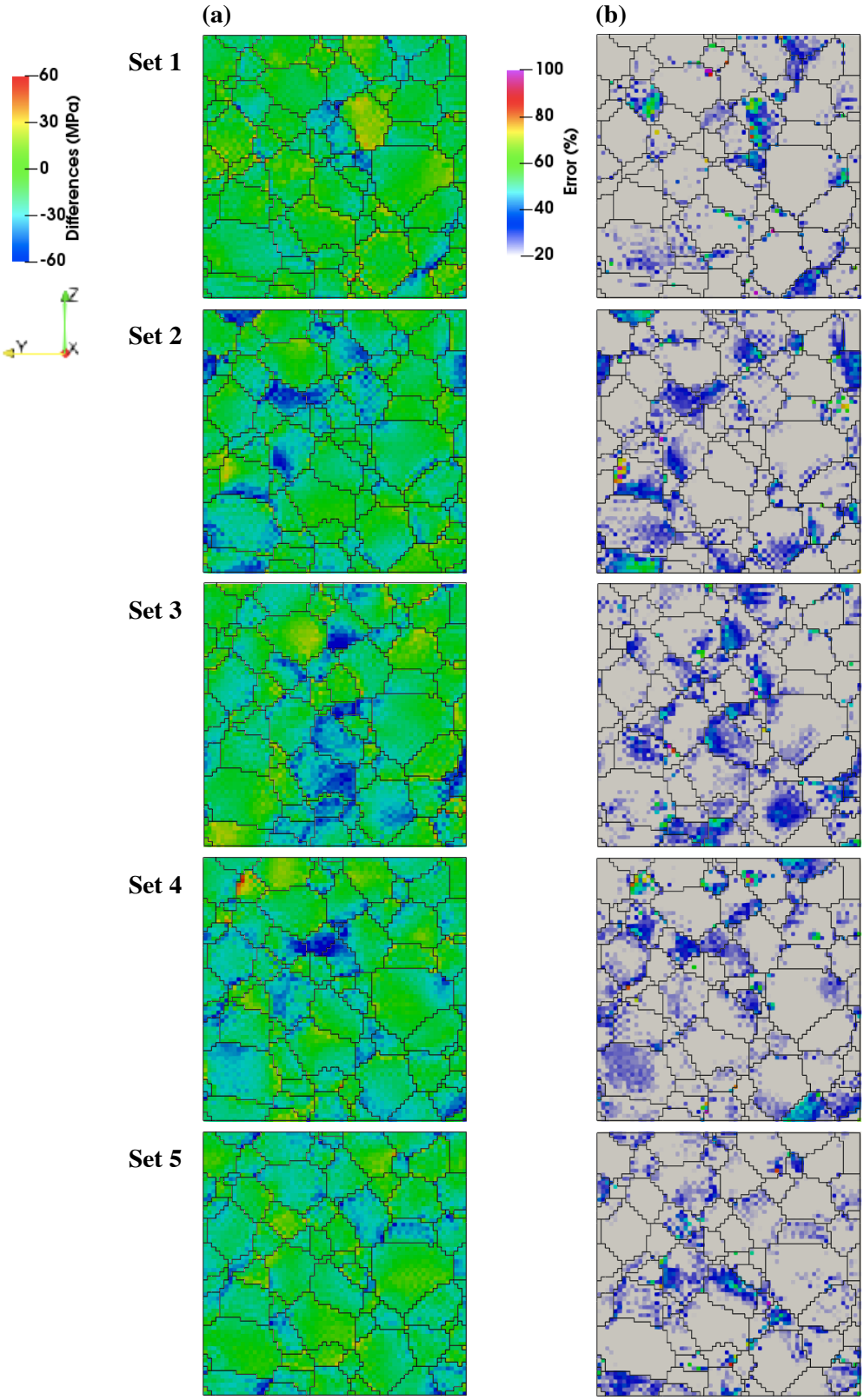

Figure 15. Calculated differences (Subtraction of TE-FFT results from TE-FEM prediction) in stress between two methods. (b) shows corresponding percent error which are calculated from absolute va lue of differences divided by stress values from FFT prediction times 100.

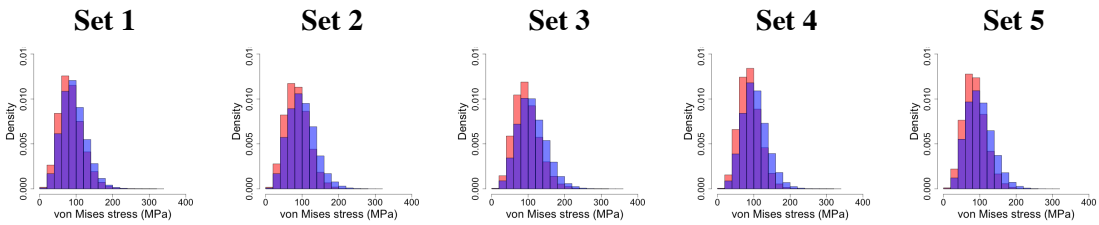

Figure 17. Probability distribution function for stress from TE-FEM (red) and TE-FFT (blue).

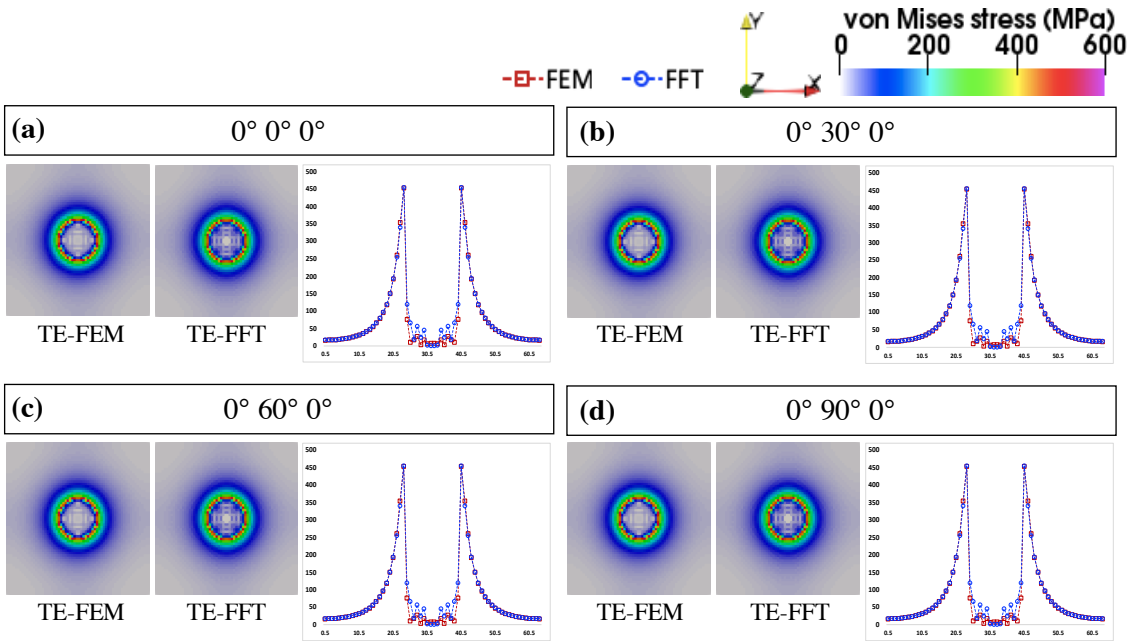

Figure 16. Stress field on cross section resulting from TE-FEM, TE-FFT (left) and relative profiles compared to Eshelby case for isotropic case.

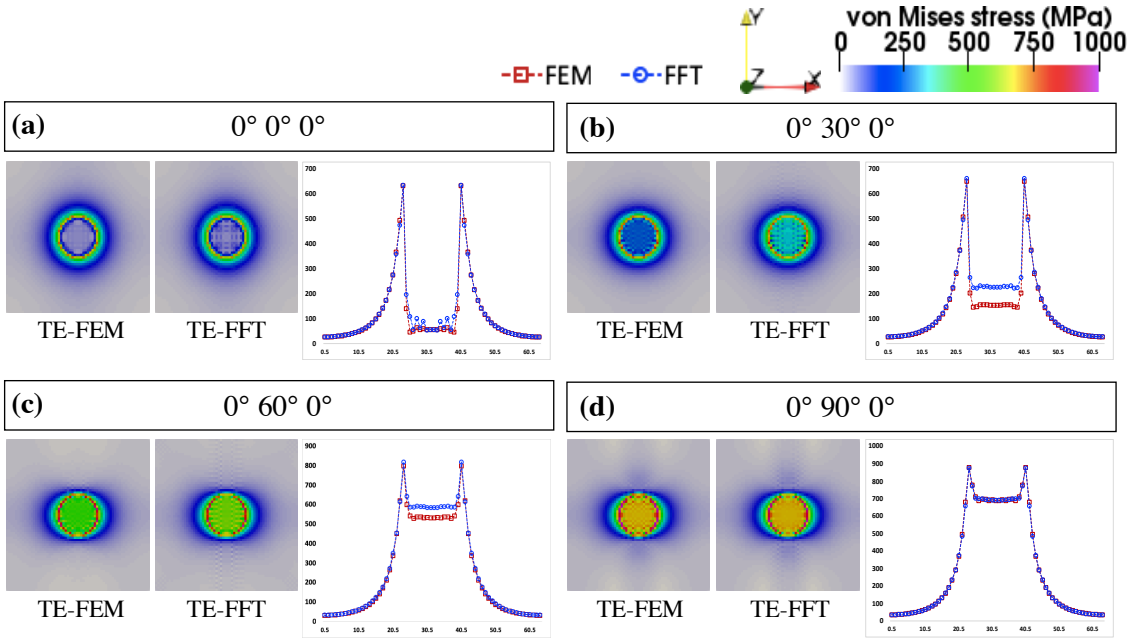

Figure 18. Stress field on cross section resulting from TE-FEM, TE-FFT (left) and relative profiles compared to Eshelby case for anisotropic case.

ULSAN NATIONAL INSTITUTE OF SCIENCE AND TECHNOLOGY

Table 5.
Descrptive statistics for stress for all five sets of test microstructure for anisotropic case.

	Ver 1		Ver 2		Ver 3		Ver 4		Ver 5	
	FEM	FFT	FEM	FFT	FEM	FFT	FEM	FFT	FEM	FFT
Mean	85.52	93.28	85.91	98.84	95.41	109.86	88.42	102.6	86	99
Min.	6.09	4.2	4.84	6.63	3.26	7.34	5.18	6.03	3.23	6.08
Max.	312.64	321.61	279.8	319.92	311.03	343.83	311.27	330.81	249.87	302.74
Std.dev.	32.54	33.72	31.87	36.89	34.68	38.85	29.36	34.18	30.19	35.9

V. Conclusion

In this research, thermoelastic response of isotropic and anisotropic polycrystalline materials between FEM and FFT were compared qualitatively and quantitatively. At first, thermoelastic responses calculated from both methods are verified by using well known analytical solution known as Eshelby problem. The accuracy of both methods improved well with increasing resolution, and such effect was much significantly appeared in FEM approach. From both calculations, stress profiles follow the Eshelby's analytical line roughly, however, deviations are still observed near interfaces between inclusion and matrix.

With respect to polycrystalline materials, both isotropic and anisotropic case were investigated. For isotropic case, stress predicted from both methods exhibit similar average value, but show differences in extreme values. Especially, large differences and errors are usually appeared in the grain boundaries and junctions. As a results of extreme value analysis, it is observed that TE-FEM predicts more and high hot spots stress than TE-FFT.

For an anisotropic case, each method exhibits different trends in mean value as well as shape of distribution. On the contrary to isotropic case, TE-FFT predicts more high stress than TE-FEM. Consequently, it is found that sensitivity to anisotropy is different according to the methods.

ULSAN NATIONAL INSTITUTE OF SCIENCE AND TECHNOLOGY

REFERENCES

[1] J. P. Carter and J. R. Booker, "Finite element analysis of coupled thermoelasticity," in *Finite Element Methods in Engineering: Proceedings of the Fifth International Conference in Australia on Finite Element Methods*, 1987: University of Melbourne, Faculty of Engineering, in association with The Institution of Engineers, Australia, p. 340.

[2] S. Donegan and A. Rollett, "Simulation of residual stress and elastic energy density in thermal barrier coatings using fast Fourier transforms," *Acta Materialia,* vol. 96, pp. 212-228, 2015.

[3] A. Kanjarla, R. Lebensohn, L. Balogh, and C. Tomé, "Study of internal lattice strain distributions in stainless steel using a full-field elasto-viscoplastic formulation based on fast Fourier transforms," *Acta Materialia,* vol. 60, no. 6-7, pp. 3094-3106, 2012.

[4] A. Prakash and R. Lebensohn, "Simulation of micromechanical behavior of polycrystals: finite elements versus fast Fourier transforms," *Modelling and Simulation in Materials Science and Engineering,* vol. 17, no. 6, p. 064010, 2009.

[5] G. Sachs, "Zur ableitung einer fliessbedingung," in *Mitteilungen der deutschen Materialprüfungsanstalten*: Springer, 1929, pp. 94-97.

[6] G.I.Taylor, "Plastic strain in metals," *Journal of the Institute of Metals,* vol. 62, pp. 307-324, 1938.

[7] D. Tjahjanto, F. Roters, and P. Eisenlohr, "Iso-Work-Rate Weighted-Taylor Homogenization Scheme for Multiphase Steels Assisted by Transformation-induced Plasticity Effect," *steel research international,* vol. 78, no. 10-11, pp. 777-783, 2007.

[8] J. D. Eshelby, "The determination of the elastic field of an ellipsoidal inclusion, and related problems," *Proc. R. Soc. Lond. A,* vol. 241, no. 1226, pp. 376-396, 1957.

[9] A. Molinari, G. Canova, and S. Ahzi, "A self consistent approach of the large deformation polycrystal viscoplasticity," *Acta Metallurgica,* vol. 35, no. 12, pp. 2983-2994, 1987.

[10] R. A. Lebensohn and C. Tomé, "A self-consistent viscoplastic model: prediction of rolling textures of anisotropic polycrystals," *Materials Science and Engineering: A,* vol. 175, no. 1-2, pp. 71-82, 1994.

[11] D. Peirce, R. Asaro, and A. Needleman, "An analysis of nonuniform and localized deformation in ductile single crystals," *Acta metallurgica,* vol. 30, no. 6, pp. 1087-1119, 1982.

[12] B. Liu, D. Raabe, F. Roters, P. Eisenlohr, and R. Lebensohn, "Comparison of finite element and fast Fourier transform crystal plasticity solvers for texture prediction," *Modelling and Simulation in Materials Science and Engineering,* vol. 18, no. 8, p. 085005, 2010.

[13] R. A. Lebensohn, A. D. Rollett, and P. Suquet, "Fast Fourier transform-based modeling for the determination of micromechanical fields in polycrystals," *Jom,* vol. 63, no. 3, pp. 13-18, 2011.

[14] R. A. Lebensohn, "N-site modeling of a 3D viscoplastic polycrystal using fast Fourier transform," *Acta materialia,* vol. 49, no. 14, pp. 2723-2737, 2001.

[15] H. Moulinec and P. Suquet, "A FFT-based numerical method for computing the mechanical properties of composites from images of their microstructures," in *IUTAM symposium on microstructure-property interactions in composite materials*, 1995: Springer, pp. 235-246.

[16] H. Moulinec and P. Suquet, "A numerical method for computing the overall response of nonlinear composites with complex microstructure," *Computer methods in applied mechanics and engineering,* vol. 157, no. 1-2, pp. 69-94, 1998.

[17] H. Moulinec, "A fast numerical method for computing the linear and nonlinear mechanical properties of composites," *C. R Acad. Sci. Paris,* vol. 318, pp. 1417-1423, 1994.

[18] J.-C. Michel, H. Moulinec, and P. Suquet, "Effective properties of composite materials with periodic microstructure: a computational approach," *Computer methods in applied mechanics and engineering,* vol. 172, no. 1-4, pp. 109-143, 1999.

[19] J.-C. Michel, H. Moulinec, and P. Suquet, "A computational method based on augmented Lagrangians and fast Fourier transforms for composites with high contrast," *CMES(Computer Modelling in Engineering & Sciences),* vol. 1, no. 2, pp. 79-88, 2000.

[20] B. Anglin, R. Lebensohn, and A. Rollett, "Validation of a numerical method based on Fast Fourier Transforms for heterogeneous thermoelastic materials by comparison with analytical solutions," *Computational Materials Science,* vol. 87, pp. 209-217, 2014.

[21] W. Leclerc, N. Ferguen, C. Pélegris, H. Haddad, E. Bellenger, and M. Guessasma, "A numerical investigation of effective thermoelastic properties of interconnected alumina/Al composites using FFT and FE approaches," *Mechanics of Materials,* vol. 92, pp. 42-57, 2016.
[22] B. F. Shorr, *Thermal Integrity in Mechanics and engineering*. Springer, 2015.
[23] J. Salem, Z. Li, and R. Bradt, "Thermal expansion and elastic anisotropy in single crystal Al2O3 and SiC whiskers," 1989.
[24] S. P. Donegan, "Spectral modeling of residual stress and stored elastic strain energy in thermal barrier coatings," Carnegie Mellon University, 2013.
[25] N.-H. Kim, *Introduction to nonlinear finite element analysis*. Springer Science & Business Media, 2014.
[26] K.-J. Bathe, *Finite element procedures*. Klaus-Jurgen Bathe, 2006.
[27] N. H. Kim, B. V. Sankar, and A. V. Kumar, *Introduction to finite element analysis and design*. John Wiley & Sons, 2018.
[28] R. Lebensohn, M. Idiart, P. P. Castañeda, and P.-G. Vincent, "Dilatational viscoplasticity of polycrystalline solids with intergranular cavities," *Philosophical Magazine,* vol. 91, no. 22, pp. 3038-3067, 2011.
[29] S. Coles, J. Bawa, L. Trenner, and P. Dorazio, *An introduction to statistical modeling of extreme values*. Springer, 2001.
[30] D. Faranda, V. Lucarini, G. Turchetti, and S. Vaienti, "Numerical convergence of the block-maxima approach to the generalized extreme value distribution," *Journal of statistical physics,* vol. 145, no. 5, pp. 1156-1180, 2011.
[31] R. L. Smith, "Estimating tails of probability distributions," *The annals of Statistics,* vol. 15, no. 3, pp. 1174-1207, 1987.
[32] A. Ferreira and L. De Haan, "On the block maxima method in extreme value theory: PWM estimators," *The Annals of statistics,* vol. 43, no. 1, pp. 276-298, 2015.
[33] B. Brabson and J. Palutikof, "Tests of the generalized Pareto distribution for predicting extreme wind speeds," *Journal of applied meteorology,* vol. 39, no. 9, pp. 1627-1640, 2000.
[34] S. Sugahara, R. P. Da Rocha, and R. Silveira, "Non-stationary frequency analysis of extreme daily rainfall in Sao Paulo, Brazil," *International Journal of Climatology: A Journal of the Royal Meteorological Society,* vol. 29, no. 9, pp. 1339-1349, 2009.
[35] V. Pisarenko and D. Sornette, "Characterization of the frequency of extreme earthquake events by the generalized Pareto distribution," *pure and applied geophysics,* vol. 160, no. 12, pp. 2343-2364, 2003.
[36] S. Beguería and S. M. Vicente-Serrano, "Mapping the hazard of extreme rainfall by peaks over threshold extreme value analysis and spatial regression techniques," *Journal of applied meteorology and climatology,* vol. 45, no. 1, pp. 108-124, 2006.
[37] P. Embrechts, C. Klüppelberg, and T. Mikosch, *Modelling extremal events: for insurance and finance*. Springer Science & Business Media, 2013.
[38] A. J. McNeil, "Extreme value theory for risk managers," *Departement Mathematik ETH Zentrum,* 1999.
[39] M. Ribatet, "A user's guide to the PoT package (version 1.4)," *University of Quebec,* 2006.
[40] J. D. Eshelby, "The elastic field outside an ellipsoidal inclusion," *Proc. R. Soc. Lond. A,* vol. 252, no. 1271, pp. 561-569, 1959.
[41] Q.-S. Zheng and D.-X. Du, "An explicit and universally applicable estimate for the effective properties of multiphase composites which accounts for inclusion distribution," *Journal of the Mechanics and Physics of Solids,* vol. 49, no. 11, pp. 2765-2788, 2001.
[42] J. Ju and L. Sun, "A novel formulation for the exterior-point eshelby's tensor of an ellipsoidal inclusion," *Journal of Applied Mechanics,* vol. 66, no. 2, pp. 570-574, 1999.
[43] T. Mura, *Micromechanics of defects in solids*. Springer Science & Business Media, 2013.
[44] A. I. H. Committee, *Properties and selection: nonferrous alloys and special-purpose materials*. Asm Intl, 1990.
[45] J. Dulieu-Barton, "Introduction to thermoelastic stress analysis," *Strain,* vol. 35, no. 2, pp. 35-39, 1999.
[46] S. Donegan, J. Tucker, A. Rollett, K. Barmak, and M. Groeber, "Extreme value analysis of tail departure from log-normality in experimental and simulated grain size distributions," *Acta Materialia,* vol. 61, no. 15, pp. 5595-5604, 2013.
[47] P. Souvatzis, O. Eriksson, and M. Katsnelson, "Anomalous thermal expansion in α-titanium," *Physical review letters,* vol. 99, no. 1, p. 015901, 2007.